MINIREVIEW

Check for updates

Bioactive metal sulfide nanomaterials as photo-enhanced chemodynamic nanoreactors for tumor therapy

Houjuan Zhu, [ID] [a] Chui Yu Chan,[a] Jerry Zhi Xiong Heng,[a] Karen Yuanting Tang,[a] Casandra Hui Teng Chai, [ID] [a] Hui Ling Tan,[b] Xian Jun Loh, [ID] *[a] Enyi Ye [ID] *[a] and Zibiao Li [ID] *[ab]

Metal sulfide nanomaterials (MeSNs) are highly promising for biomedical applications due to their low toxicity, good dispersibility, high stability, adjustable particle sizes, and good biocompatibility. Their unique chemical and light-conversion properties also enable them to function as photothermal or photodynamic agents, enhancing chemodynamic therapy (CDT) of tumors. This makes MeSNs valuable as photo-enhanced CDT nanoagents, advancing precision and multi-modal tumor treatment. This review examines recent advancements in MeSNs for photo-enhanced chemodynamic tumor ablation, comparing their effectiveness in CDT. It highlights the roles of photothermal, photodynamic, and photocatalytic effects in enhancing treatment efficacy. MeSN-based nanoreactors are categorized by composition into iron sulfide, copper sulfide, other unary, and multi-MeSNs for their applications in tumor therapy. Additionally, this review discusses challenges, limitations, and future biomedical applications of MeSNs, offering insights into their potential for next-generation cancer treatments.

1. Introduction

Tumors pose a significant and growing threat to human health, claiming millions of lives annually with an alarming upward trend in incidence and mortality rates. Traditional treatment methods such as surgery, chemotherapy (CHT), precision oncology,[1–3] and radiotherapy (RT) have long been the cornerstone of cancer management.[4–9] However, their efficacy is often undermined by severe side effects and complications, which limit their widespread application and impact patients' quality of life. In response to these challenges, a variety of nano-medicine-based innovative tumor treatment modalities have emerged in recent years.[10,11] These include chemodynamic therapy (CDT),[12] which exploits tumor microenvironment (TME)-specific catalytic reactions to produce toxic reactive oxygen species (ROS); photodynamic therapy (PDT),[13–15] which uses light-activated agents to induce cellular damage; photothermal therapy (PTT),[16,17] which relies on localized heat generation to ablate tumors; sonodynamic therapy (SDT),[18] which employs ultrasound to

activate therapeutic agents; and starvation therapy (ST) that disrupts the nutrient supply essential for tumor growth.[19–21] Collectively, these advanced approaches represent a paradigm shift in oncology, offering targeted and less invasive alternatives to conventional treatments.

Chemodynamic therapy (CDT) has recently emerged as a groundbreaking cancer treatment strategy, garnering attention for its innovative mechanism and significant potential advantages.[22] It leverages the unique TME to catalyse reactions that selectively destroy cancer cells. Specifically, CDT utilizes iron or other transition metal ions (such as Cu, Co, Mn, *etc.*) to convert excess hydrogen peroxide (H_2O_2) in tumors into highly cytotoxic hydroxyl radicals ($^\bullet OH$) through Fenton/Fenton-like reactions under acidic conditions.[23] These $^\bullet OH$ radicals induce oxidative stress, which disrupts critical cellular processes like DNA replication and protein function, ultimately triggering cancer cell apoptosis.[24,25] CDT offers several notable benefits over traditional therapies. It is a non-invasive treatment modality with high tumor selectivity and minimal side effects. The tumor-specific selectivity is rooted in the acidic nature of the TME and the elevated H_2O_2 levels within cancer tissues.[26] In contrast, noncancerous regions, which typically exhibit a neutral or alkaline pH and lower H_2O_2 concentrations, are less affected because Fenton/Fenton-like reactions are challenging to initiate under these conditions. This precise targeting minimizes off-target toxicity, addressing a major limitation of many

[a] *Institute of Materials Research and Engineering, Agency for Science, Technology and Research (A*STAR), 2 Fusionopolis Way, 138634, Singapore. E-mail: lohxj@imre.a-star.edu.sg, yeey@imre.a-star.edu.sg, lizb@imre.a-star.edu.sg*

[b] *Institute of Sustainability for Chemicals, Energy and Environment (ISCE2) A*STAR (Agency for Science, Technology and Research), Singapore 138634, Singapore*

conventional cancer therapies. Moreover, unlike PDT, CDT does not rely on external factors such as oxygen availability or laser irradiation.[27–29] This independence makes it particularly advantageous for treating hypoxic tumors, which are resistant to oxygen-dependent treatments. These unique properties make CDT a promising alternative for more targeted cancer treatment.

Despite its potential, several challenges hinder the clinical application of CDT: (1) low endogenous H_2O_2 levels limit the Fenton/Fenton-like reactions for effective ROS production in many tumors;[15,30–32] (2) mild tumor acidity (pH 5.6–6.8) decreases the catalytic efficiency of Fenton/Fenton-like reactions;[33] (3) high glutathione (GSH) concentration enhances $^{\bullet}OH$ scavenging and reduces oxidative stress, thereby diminishing the therapeutic efficacy of CDT.[34] To overcome these limitations, researchers have explored various strategies to improve CDT's effectiveness. One of the most promising approaches is combining CDT with other therapeutic modalities to create synergistic effects. In particular, phototherapy including PTT and PDT complements CDT by enhancing ROS production and reaction kinetics.[15,27,30] The localized heat from PTT accelerates the reaction rate of Fenton/Fenton-like processes, boosting $^{\bullet}OH$ production. PDT generates additional ROS, further amplifying oxidative stress within the tumor. By integrating CDT with phototherapy, the nanocatalytic efficiency of Fenton/Fenton-like reactions can be significantly enhanced.[35,36] This synergistic approach improves the overall therapeutic impact by generating higher ROS concentrations and accelerating reaction kinetics. While CDT and its combination strategies show great promise, continued innovation is necessary to address current limitations. Enhancing the catalytic efficiency of CDT agents, increasing endogenous H_2O_2 availability, and reducing tumor GSH levels are critical research directions. With ongoing advancements in nanomaterial engineering and therapeutic integration, CDT has the potential to become a cornerstone of next-generation cancer treatment, offering targeted and minimally invasive options for improved patient outcomes.

In line with this principle of Fenton/Fenton-like reaction, most CDT nanoagents are designed as metal-containing bioactive nanomaterials, including metal–organic frameworks,[37–40] metal sulfides,[28,41–44] metal carbides,[36] and metal oxides.[45–47] These nanomaterials play a crucial role in catalysing ROS production, thereby enhancing the therapeutic impact of CDT. Recently, these metal-based nanoagents have attracted significant attention in biomedical research due to their ability to amplify the efficacy of various therapeutic approaches. Among the diverse types of CDT nanoagents, MeSNs stand out as particularly promising for biomedical applications.[48–51] Their exceptional physical properties – such as low toxicity, excellent dispersibility in biological environments, high physiological stability, and tunable particle size-make them highly biocompatible and effective in clinical settings. Beyond their favorable physical attributes, MeSNs exhibit a range of notable chemical characteristics that are instrumental in therapeutic applications. For instance, their Fenton-like catalytic activity enables efficient ROS generation, which is critical for inducing oxidative damage in tumor cells. Additionally, MeSNs

possess unique light-conversion properties, allowing them to serve as both photothermal and/or photodynamic agents for enhanced chemodynamic cancer therapies. In summary, the combination of their distinctive physical and chemical properties makes MeSNs an invaluable tool as photo-enhanced CDT nanoagents in the field of tumor treatment, where they contribute to significant advancements in precision and multi-modal therapeutic approaches.

To date, although a growing number of research studies have explored the use of MeSNs for tumor therapy,[19,52–54] and a growing body of reviews have systematically summarized their applications in therapy, imaging, and drug delivery, a comprehensive and detailed overview specifically addressing the application of MeSNs in CDT for tumors is still notably absent. This review aims to address this gap by providing an in-depth examination of recent advances in the use of MeSNs for photo-enhanced chemodynamic-induced tumor ablation (Fig. 1). It summarizes and compares various types of MeSNs employed in photo-enhanced CDT of tumors (Table 1). According to relevant references, the photothermal, photodynamic, and photocatalytic effects of MeSNs are individually analysed, highlighting their role in improving CDT efficacy against tumors. These mechanisms are further clarified in terms of their respective contributions, including heat-accelerated ROS generation rates and external energy-driven increases in ROS concentrations. Furthermore, based on their synthetic composition, photo-enhanced chemodynamic nanoreactors are categorized into iron sulfide nanomaterials, copper sulfide nanomaterials, other unary MeSNs, and binary MeSNs. The application of each category in photo-enhanced CDT for cancer is discussed and emphasized in detail. Finally, this review not only addresses the current limitations and potential challenges of MeSNs as CDT nanoagents but also explores their future prospects and broader applications in other biomedical fields.
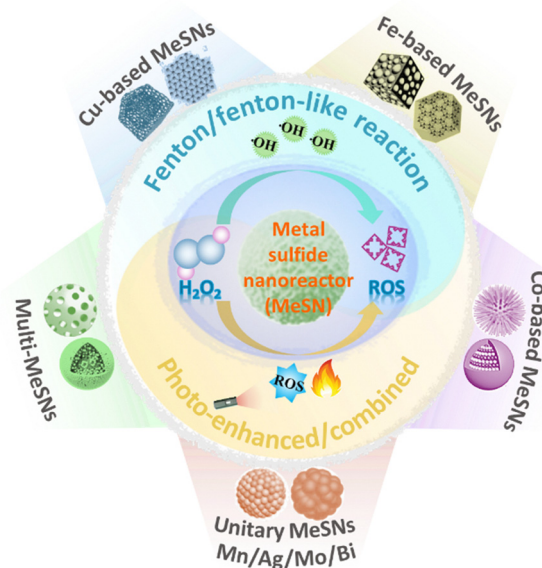

Fig. 1 Photo-enhanced chemodynamic therapeutics of tumor by metal sulfide nanomaterials (MeSNs).

Table 1 Photo-enhanced chemodynamic therapeutics for tumors using metal sulfide nanomaterials (MeSNs)

Nanomaterials	Composition	Size (nm)	PCE (%)	Irradiation conditions	Cell line/animal model	Treatment/imaging	Ref.
FeS$_x$-based nanomaterials	PEG-FeS$_2$ NCs	180–200	28.6	808 nm, 1.5 W cm^{-2}, 0.33 W cm^{-2}	4T1 cells, 4T1 tumor-bearing mice	PTT-CDT/MRI	26
	Sa@FeS	NA	29.6	1064 nm, 1.5 W cm^{-2}	4T1 tumor-bearing mice	CDT	65
	Carbon@FeS$_2$	~125	27.2	808 nm, 1.5 W cm^{-2}	HeLa cells, HeLa tumor-bearing mice	PTT-CDT/US-PAI-MRI	66
	FeS-PEG-CAI NPs	~20	56.51	1064 nm, 1.0 W cm^{-2}	HeLa tumor-bearing mice	PTT-CDT-GT/PAI-MRI-US	67
	BSO-FeS$_2$ NPs	~7.27	49.5	808 nm, 1.0 W cm^{-2}	4T1 cells, 4T1 tumor-bearing mice	PTT-PDT-CDT/PAI	68
	FeS$_2$@SRF@BSA NPs	~100	NA	808 nm, 1.0 W cm^{-2}	4T1 cells, 4T1 tumor-bearing mice	PTT-PDT-CDT/FLI	69
	FeS-GOx NDs	~12	NA	808 nm, 1.8 W cm^{-2}, 1.6 W cm^{-2}	4T1 cells, 4T1 tumor-bearing mice	PTT-CDT/US-PAI-MRI	70
	BSA-FeS$_2$ NPs	163.0–212.4	29.7	1064 nm, 1.0 W cm^{-2}	4T1 cells, 4T1 tumor-bearing mice	PTT-CDT-ICD	72
	PVP-Fe$_3$S$_4$ NSs	~120, 15–25	64.3	915 nm, 0.5 W cm^{-2}	HeLa, SKO-V3 cells, HeLa tumor-bearing mice	PTT-CDT/MRI	73
	PEG-Fe$_3$S$_4$ NPs	~20	45	1064 nm, 1.5 W cm^{-2}	4T1, SH-SY5Y cells, SH-SY5Y tumor-bearing mice	PTT-CDT/PAI	74
CuS$_x$-based nanomaterials	PEG-Cu$_{2-x}$S NDs	2–5	30.8	1064 nm, 1.5 W cm^{-2}	4T1 cells, 4T1 tumor-bearing mice	PTT-CDT/PAI	79
	AIBA@CuS-FA NPs	~13	47.5	1064/808 nm, 0.5 W cm^{-2}	KB cells, KB tumor-bearing mice	PTT-PDT-CDT	80
	GOx@CuS nanocomposites	~8	NA	808 nm, 1.0 W cm^{-2}	B16F10, MDA-MB-231 cells, B16F10 tumor-bearing mice	PTT-PDT-CDT-ST	81
	Cu-MOF	~85	45.7	808 nm, 1.0 W cm^{-2}	L929, HeLa, CT26 cells, CT26 tumor-bearing mice	PTT-CDT	89
	PVP-Cu$_9$S$_8$ NPs	~36.3	NA	1064 nm, 0.2 W cm^{-2}	4T1 cells, 4T1 tumor-bearing mice	PTT-CDT/PAI	82
	CuS@COFs-BSA-FA/DOX	~300	21.5	808 nm, 1.0 W cm^{-2}	4T1 cells, 4T1 tumor-bearing mice	PTT-CDT-CHT	90
	Cu$_9$S$_8$ NPs	~18.05	NA	808 nm, 1.0 W cm^{-2}	4T1 cells, 4T1 tumor-bearing mice	PTT-CDT/PAI	91
	CCM-Lap-CuS NPs	~3.3	NA	1064 nm, 1.0 W cm^{-2}	4T1, RAW264.7 cells, 4T1 tumor-bearing mice	PTT-CDT/FLI-PAI	92
	hollow mesoporous CuS NPs	~130	22.5	808 nm	LO-2, MCF-7, A549, MDA-MB-231 cells, MCF-7 tumor-bearing mice	PTT-CDT	93
	HCuS NPs-HCQ-PEG	~170 by DLS	46	1060 nm, 1.0 W cm^{-2}	4T1 cells, 4T1 tumor-bearing mice	PTT-CDT/PAI	94
	D-HCuS@HA	~177.9 by DLS	NA	808 nm, 2.0 W cm^{-2}	4T1 cells, 4T1 tumor-bearing mice	PTT-CDT-CHT/FLI	95
	CuS-ICG@PDA-FA NPs	~210.5	61.2	808 nm, 0.8 W cm^{-2}	4T1 cells, 4T1 tumor-bearing mice	PTT-PDT-CDT/FLI	96
	DOX@H-Cu$_9$S$_8$-PEG NPs	~100	40.9	1064 nm, 1.0 W cm^{-2}	HUVEC, CT26 cells, CT26 tumor-bearing mice	PTT-CDT-CHT	97
	HM-CuS-HA(GOx)-Lf NPs	~50	NA	808 nm, 1.0 W cm^{-2}	C6 cells, C6 tumor-bearing mice	PTT-CDT-ST-CHT/CT-MRI	99

Table 1 (continued)

Nanomaterials	Composition	Size (nm)	PCE (%)	Irradiation conditions	Cell line/animal model	Treatment/imaging	Ref.
	DOX/CuS@Cu-MOF/PEG nanocomposites	Lengths: ~200; widths: ~40	39.6	1064 nm, 1.0 W cm^{-2}	4T1 cells	PTT-CDT-CHT/PAI	100
	HP-PCN@CuS nanoplatform	5–20	42.3	808 nm, 1.0 W cm^{-2}	4T1 tumor-bearing mice	PTT-PDT-CDT	101
	SiO$_2$@Cu$_9$S$_4$ NCs	5–8	30.3	808 nm, 1.3 W cm^{-2}	4T1, HepG2, Caco-2, L02 cells; 4T1 tumor-bearing mice	PTT-PDT-CDT	102
	PS@Cu$_9$S$_8$ nanocatalysts	~156.1 by DLS	42.34	1064 nm, 1.5 W cm^{-2}	HeLa cells; HeLa tumor-bearing mice	PTT-CDT	103
	Cu$_9$S$_5$ NSs	2–3	58.96	808 nm, 1.0 W cm^{-2}; 1064 nm, 1.0 W cm^{-2}	4T1 cells; 4T1 tumor-bearing mice	PTT-CDT	104
	CuS@G5-PEG NPs	~25	NA	808 nm, 1.2 W cm^{-2}	3T3, 4T1 cells; 4T1 tumor-bearing mice	PTT-CDT	105
	Alg-CuS/BSA NPs	~22	NA	808 nm, 1.0 W cm^{-2}	4T1 cells; 4T1 tumor-bearing mice	PTT-PDT-CDT	106
	CuS NPs	~196 by DLS	NA	808 nm, 0.5 W cm^{-2}	4T1 cells	PTT-CDT-CHT	107
	CuS-GOx NPs	~8	NA	850 nm	CT26 cells; CT26 tumor-bearing mice	PTT-CDT-ST	108
	Fuc-CuS NPs-DOX	10–20	39.77	1.5 W cm^{-2}	MDA-MB-231, A375, HEK-293 cells; A375 tumor-bearing mice	PTT-CDT/CT	110
	Hollow CuS NPs	NA	30	808 nm, 1.0 W cm^{-2}	B16F10 cells; B16F10 tumor-bearing mice	PTT-CDT	111
	Liposome-Cu-GOx nanocarriers	~56.46 by DLS	33.8	808 nm, 0.5 W cm^{-2}	A549 cells; A549 tumor-bearing mice	PTT-CDT	112
	AG@Cu$_9$S$_8$@dOMV	~161	44.35	1064 nm, 1.0 W cm^{-2}; 1064 nm, 1.0 W cm^{-2}	CT26 cells; CT26 tumor-bearing mice; GI261 cells; GI261 tumor-bearing mice	PTT-CDT-ST-CHT/FLI	113
CoS$_x$-based nanomaterials	CoS$_2$ NCs	~19.79	60.4	808 nm, 1.0 W cm^{-2}, 0.75 W cm^{-2}	4T1 cells; 4T1 tumor-bearing mice	PTT-CDT/PAI	115
	Co$_{2.19}$S$_4$ NDs	3–5	52	880 nm, 1.0 W cm^{-2}	4T1, 3T3 cells; 4T1 tumor-bearing mice	PTT-CDT-ST	116
	BSA-CoS$_x$ QDs	~5.8	40.5	808 nm, 0.8 W cm^{-2}	A431, 4T1 cells; 4T1 tumor-bearing mice	PTT-CDT	117
	ZIF@Co$_3$S$_4$-ICG	~254	40.5	808 nm, 1.0 W cm^{-2}	4T1 cells; 4T1 tumor-bearing mice	PTT-PDT-CDT	118
	GOx@PCoS	~180	45.06	808 nm, 1.0 W cm^{-2}	4T1 cells; 4T1 tumor-bearing mice	PTT-PDT-CDT/MRI	119
Other unitary-metal sulfide-based nanomaterials	MnS@PDA	~100	24.48	808 nm, 1.5 W cm^{-2}	LLC, HUVEC, 3T3 cells; LLC tumor-bearing mice	PTT-CDT/MRI-FLI	124
	Bi$_2$S$_3$@Bi@PDA-HA/Art NRs	~120; ~30	23.35	808 nm, 1.0 W cm^{-2}	4T1 cells; 4T1 tumor-bearing mice	PTT-PDT-CDT	125
	PEG-Ag$_2$S-Ag	~17	56.8	808 nm, 2.0 W cm^{-2}, 1.0 W cm^{-2}	L929, HeLa cells; HeLa tumor-bearing mice	PTT-CDT/FLI	128
Multi-metal sulfide-based nanomaterials	Cu$_2$ZnSnS$_4$@BSA	~12.6 by DLS	31.6	808 nm, 1.0 W cm^{-2}	HepG-2 cells; H22 tumor-bearing mice	PTT-CDT/MRI-PAI	151

Table 1 (continued)

Nanomaterials Composition	Size (nm)	PCE (%)	Irradiation conditions	Cell line/animal model	Treatment/imaging	Ref.
$Ag_2S\text{-}Cu(II)\text{-}Cu_{2-x}Se$ NPs	34.2	61.2	808 nm 1.0 W cm^{-2}	L929, MRC-5, HeLa cells	PTT-CDT	127
$Zn_xMn_{1-x}S@PDA$	~280	32.79	808 nm	HUVECs, L02, L929, CT26, HeLa, 4T1 cells	PTT-CDT	129
			2.0 W cm^{-2}, 1.0 W cm^{-2}	4T1 tumor-bearing mice		130
$TPZ@Cu\text{-}SnS_{2-x}/PLL$	~300	32.8	808 nm 0.8 W cm^{-2}	L929, 4T1 cells 4T1 tumor-bearing mice	PTT-CDT-CHT/CT-PAI	130
$PEG\text{-}Cu_5FeS_4$ NPs	~22	45.9	1064 nm 1.0 W cm^{-2}	4T1 cells 4T1 tumor-bearing mice	PTT-CDT/MRI	131
Mn doped Cu_7S_4 NPs	~90	40.3; 33.4	808 nm 1.5 W cm^{-2} 1064 nm 1.5 W cm^{-2}	BV-2, PC3, HeLa cells HeLa tumor-bearing mice	PTT-CDT-CHT	132
BSA-Ag:CuS NPs	~67	37.8	1064 nm 1.25 W cm^{-2}	4T1 cells 4T1 tumor-bearing mice	PTT-CDT	133
$Co_{3-x}Cu_xS_4$ NPs	~250	46.7	808 nm 1.0 W cm^{-2}	L929, 4T1 cells 4T1 tumor-bearing mice	PTT-CDT	134
BiNS-Fe@Fe-PVP	48.6	37.9	808 nm 1.31 W cm^{-2}	HepG-2, Eca109 cells HepG-2 tumor-bearing mice	PTT-PDT-CDT/CT-MRI-PAI	135
Mn-CoS@carbon-BSA-DOX	~50	66.3	808 nm 0.75 W cm^{-2}	HepG-2 cells H22 tumor-bearing mice	PTT-CDT/MRI-CT	136
$CoSnS_2$ NCs	~320	47.23	808 nm 1.5 W cm^{-2}	L02, HUVECs, HC11, 4T1 cells 4T1 tumor-bearing mice	PTT-CDT	137
$PEG\text{-}MoS_2/Co_3S_4$ NFs	100–150	39.8	1064 nm 0.8 W cm^{-2}	HepG-2, NCM 460 cells 4T1 tumor-bearing mice	PTT-PDT-CDT/MRI	138
$PEG\text{-}FeS_2/CoS_2$ NSs	~80	50.5	1064 nm 0.8 W cm^{-2}	HepG-2 cells HepG-2 tumor-bearing mice	PTT-PDT-CDT/MRI-CT	139
$PVP\text{-}NiS_2/FeS_2$ NPs	NA	36.74	808 nm 1.0 W cm^{-2}	4T1 cells 4T1 tumor-bearing mice	PTT-PDT-CDT/MRI-PAI	140
$PEG\text{-}Cu_2MoS_4$ @GOx	~142.5 by DLS	63.3	1064 nm 0.48 W cm^{-2}	L929, HeLa cells U14 tumor-bearing mice	PTT-PDT-CDT-ST	141
$PEG\text{-}Cu_xMn_yS_z$	~140	56.7	1064 nm 1.0 W cm^{-2}	4T1 cells 4T1 tumor-bearing mice	PTT-CDT/MRI-PAI	143
$PEG\text{-}CuMo_2S_3$ NPs	~230	38.2	1064 nm 0.68 W cm^{-2}	B16-F10 cells	PTT-PDT-CDT	145
$BSA\text{-}CuFeS_2$ NPs	~4.9	38.8	808 nm 1.5 W cm^{-2}	4T1 cells 4T1 tumor-bearing mice	PTT-CDT/MRI-FLI	148
CuS-Fe@polymer	~100	NA	808 nm 0.5 W cm^{-2}, 0.75 W cm^{-2}	HeLa, NIH3T3 cells 4T1 tumor-bearing mice	PTT-CDT	149
$Bi_2S_3@Fe/Mn\text{-}ZIF\text{-}8/MTX$	~259 by DLS	54	808 nm 0.75 W cm^{-2}	HepG2 cells HepG2 tumor-bearing mice	PTT-CDT-CHT/MRI-CT	152
$DOX@Fe(III)@WS_2\text{-}PVP$	~108	39.1	808 nm 1.0 W cm^{-2}	HT29 cells HT29 tumor-bearing mice	PTT-CDT-CHT	153
PEI-CuMnS NPs	~20	67.8	808 nm 1.0 W cm^{-2}	4T1 cells 4T1 tumor-bearing mice	PTT-PDT-CDT	154

2. Overview of MeSN-based photo-enhanced chemodynamic nanoreactors

2.1 Synthesis methods, *in vivo* metabolic pathways, and long-term toxicity of MeSNs

Metal sulfide nanomaterials (MeSNs) have garnered significant attention due to their diverse applications, particularly in biomedical fields. Various synthesis methods, including co-precipitation, hydrothermal synthesis, and sol–gel processes, enable precise control over particle size and morphology-critical factors for optimizing their properties. Recently, environmentally friendly green synthesis approaches using plant extracts or microbial systems have gained interest as sustainable alternatives that minimize the use of toxic chemicals. Furthermore, surface functionalization techniques such as PEGylation or ligand attachment enhance the biocompatibility and targeting capabilities of MeSNs, thereby improving therapeutic efficacy while reducing potential side effects.

Also, MeSNs after administration undergo complex *in vivo* metabolic processes that influence their biodistribution, metabolism, and biodegradation. Factors such as particle size, surface charge, and functionalization impact their distribution across tissues and organs, with the liver, spleen, and kidneys being primary accumulation sites. These organs play essential roles in nanoparticle metabolism and excretion, making it crucial to understand these pathways to predict the long-term biological behavior of MeSNs. Additionally, certain MeSNs can undergo biodegradation, releasing metal ions that may interact with biological systems, requiring further investigation into their therapeutic potential and associated toxicity.

Assessing the long-term toxicity of MeSNs is vital to ensure their safety for biomedical use. Toxicological evaluations, including acute and chronic toxicity studies, examine potential impacts on organ function, histopathology, and overall physiological health. One major concern is the release of metal ions, which may induce cytotoxic effects if present at harmful concentrations. Besides, MeSNs can provoke immune responses, potentially leading to chronic inflammation or other adverse effects. Comprehensive research on these aspects is necessary to mitigate risks and optimize the biocompatibility of MeSNs.

A thorough understanding of the synthesis methods, *in vivo* metabolic pathways, and long-term toxicity of MeSNs is essential for their safe and effective biomedical applications. Continued research in these areas will contribute to the advancement of targeted therapies, ultimately improving patient outcomes in cancer treatment and beyond.

2.2 Influence of metal elements on MeSN properties

Metal sulfide nanomaterials (MeSNs) have been widely reported in biomedical applications due to their highly tunable physicochemical performances, which are primarily dictated by the type of incorporated metal cation. Factors such as the metal's electronic configuration, oxidation state, coordination environment, and ionic radius play a crucial role in shaping the

Table 2 Summary of MeSNs' physicochemical properties for bioapplication

MeSNs	Properties
FeS_x	Magnetic properties, Fenton catalytic effect
CuS_x	Fenton-like catalytic, localized surface plasmon resonance (LSPR)
CoS_x	Fenton-like catalytic, electrocatalytic performance, magnetic properties
AgS_x	NIR-II fluorescence, localized surface plasmon resonance (LSPR), antibacterial properties
MnS_x	T_1-weighted MRI contrast ability, modulating oxidative stress, redox-mediated catalytic activity
MoS_x	Photothermal, photodynamic and photocatalytic properties, redox-mediated catalytic activity
NiS_x	Electrocatalytic activity, magnetically responsive properties
BiS_x	Strong X-ray attenuation, photothermal properties

nanoparticles' morphology, crystallinity, surface charge, optical characteristics, biodegradability, and biocompatibility. These structural and chemical variations directly impact their suitability for diverse biomedical applications, ranging from therapeutics and imaging to biosensing and drug delivery. This section explores the distinctive properties of unitary MeSNs, including CuS_x, FeS_x, CoS_x, AgS_x, MnS_x, MoS_x, NiS_x, and BiS_x, with a focus on their biomedical relevance. A detailed comparative summary of these materials is provided in Table 2, highlighting their key physicochemical attributes to show the potential applications.

Beyond unitary MeSNs, multi-metal sulfide nanomaterials (MMeSNs), such as $CuFeS_2$, $CoSnS_2$, Cu_2MoS_4, $CuMnS$, and Cu_2ZnSnS_4, have been engineered to harness the synergistic advantages of multiple metal cations within a single nanostructure. By integrating different metal ions, these heterostructured materials exhibit enhanced photothermal conversion efficiency, improved catalytic activity, superior magnetic responsiveness, and increased structural stability, broadening their functional versatility in biomedical applications. MMeSNs facilitate multi-modal therapeutic strategies, including simultaneous bioimaging, targeted drug delivery, and combination therapies, such as PTT, PDT, and CDT. Also, their improved electronic and optical properties, attributed to bandgap modulation and electron transfer effects, position them as highly promising candidates for applications in photoacoustic imaging (PAI), fluorescence-guided diagnostics, and TME modulation. However, despite these advantages, the complexity of MMeSN synthesis, which often requires precise control over stoichiometry, crystal phase, and heterojunction formation, poses significant challenges. Furthermore, the potential toxicity and bioaccumulation risks associated with the release of multiple metal ions necessitate systematic cytotoxicity evaluations, *in vivo* biodistribution studies, and long-term biocompatibility assessments to guarantee their clinical safety.

The biomedical performance of MeSNs is highly dependent on the intrinsic chemical and physical characteristics of the incorporated metal ions. Each metal confers specific functional attributes, such as localized surface plasmon resonance (LSPR) in CuS_x and AgS_x, magnetic properties in FeS_x and CoS_x, redox-mediated catalytic activity in MoS_x and MnS_x, and high X-ray

attenuation in BiS_x, all of which can be strategically leveraged for targeted therapies, advanced bioimaging techniques, and theranostic applications. However, critical variations in toxicity, ion release kinetics, and biodegradability necessitate careful material optimization, surface engineering, and systematic biocompatibility assessments. While MMeSNs present a promising avenue for next-generation biomedical applications, further mechanistic studies are essential to fully elucidate their biological interactions, metabolic pathways, and long-term toxicity profiles. Advancements in their nanomaterial synthesis, functionalization strategies, and controlled drug delivery systems will be pivotal in accelerating their clinical translation and regulatory approval for safe and effective biomedical applications.

2.3 Mechanism of photo-enhanced chemodynamic effects

In light of the above summary, it is evident that while MeSN-based CDT offers substantial advantages over conventional cancer treatments, such as high specificity, minimal invasiveness, and the ability to exploit the unique TME,[55] it remains limited in its clinical applications due to several inherent challenges. These challenges include suboptimal catalytic activity under physiological conditions,[30,56] insufficient production of ROS required for effective tumor destruction,[57,58] and the presence of intracellular antioxidants like GSH, which can neutralize ROS and mitigate the therapeutic efficacy of CDT.[43,59] To address these limitations and maximize the therapeutic potential of MeSN-based CDT, researchers have developed an array of innovative strategies aimed at overcoming these barriers.[60–63] These strategies are largely focused on three interconnected objectives:

(1) Designing highly efficient MeSN-based CDT agents: recent advances in nanotechnology have enabled the creation of MeSNs with superior catalytic properties. By engineering nanomaterials with enhanced surface area, higher reactivity, and optimized compositions, these CDT agents demonstrate improved efficiency in catalysing reactions that produce ROS, even under the relatively mild conditions of the TME.

(2) Optimizing environmental conditions: tumors exhibit distinct microenvironmental characteristics, such as hypoxia, acidity (low pH), and high levels of reducing agents like GSH. These unique properties can be exploited to improve CDT performance. By developing MeSNs that respond to acidic pH or modulating environmental factors such as temperature, researchers aim to amplify the catalytic reactions and boost the production of ROS directly within the tumor.

(3) Amplifying oxidative stress in tumors: enhancing oxidative stress within tumors is critical for effective CDT. Strategies to increase ROS levels include elevating the availability of H_2O_2, a key substrate for Fenton and Fenton-like reactions, or depleting GSH, which acts as an antioxidant and scavenges ROS. By tipping the redox balance in favor of oxidative damage, these approaches improve the overall efficacy of CDT.

Among these strategies, light activation has emerged as a highly promising technique due to its ability to achieve precise, localized treatment while minimizing off-target effects. Light activation leverages the unique properties of specific wavelengths, particularly within the near infrared (NIR)-I biological window (650–950 nm), which allows for deep tissue penetration and low absorption by healthy tissues. This makes it an ideal candidate for enhancing the performance of MeSN-based CDT. Light activation enhances the catalytic efficiency of MeSNs by triggering or amplifying chemical reactions that generate ROS. This process is particularly advantageous because it allows for spatiotemporal control over the activation of MeSNs, ensuring that therapeutic effects are confined to the tumor site. Furthermore, by reducing the required dosage or the need for extreme conditions, light activation minimizes potential side effects and improves the overall safety profile of the therapy. Upon exposure to light, MeSNs absorb energy and utilize it to catalyse the production of ROS, which are crucial for inducing oxidative stress and destroying cancer cells. This enhancement in ROS production occurs through two main mechanisms: (1) photothermal effects: light absorption by MeSNs generates heat, which accelerates Fenton/Fenton-like reactions. These reactions involve the reduction of transition-metal ions from a higher valence state to a lower one, facilitating the rapid decomposition of H_2O_2 into highly reactive $^{\bullet}OH$. Additionally, the heat generated during the photothermal process promotes the conversion of intracellular GSH into its oxidized form (GSSG). This depletes the tumor's antioxidant defences, further increasing oxidative stress. To better understand these processes, Fig. 2A depicts photothermal-triggered electron transfer and thermal activation of the Fenton catalytic cycle. These visualizations can help clarify the interplay between thermal energy, redox activity, and ROS production at the nanoscale. Moreover, integrating theoretical approaches – such as density functional theory (DFT) calculations or molecular dynamics simulations – could provide valuable insights into activation energy barriers, electron density redistribution, and transition-state dynamics under photothermal stimulation. These combined experimental and computational strategies will be instrumental in advancing the mechanistic understanding of light-enhanced CDT and in guiding the rational design of next-generation nanocatalysts for synergistic cancer therapy; (2) photodynamic and photocatalytic effects: in addition to the photothermal effects, light-activated MeSNs can act as photosensitizers to generate singlet oxygen ($^1O_2$) through energy transfer to molecular oxygen. Simultaneously, they can function as photocatalysts, producing superoxide ions ($O_2^{\bullet-}$) and $^{\bullet}OH$ from water via photochemical reactions. These additional ROS species further amplify the oxidative damage inflicted on cancer cells.

As depicted in Fig. 2B, the combined effects of heat and light activation significantly enhance the therapeutic outcomes of MeSN-based CDT. Heat generated by light activation not only accelerates the catalytic conversion of H_2O_2 into ROS but also disrupts the tumor's redox balance by depleting GSH. At the same time, light-driven photodynamic and photocatalytic processes contribute to the production of various ROS species, including $^1O_2$, $O_2^{\bullet-}$, and $^{\bullet}OH$, further intensifying oxidative stress within cancer cells. Collectively, these mechanisms demonstrate the immense potential of light activation as a versatile and effective strategy for improving the performance of MeSN-based CDT. By integrating light-responsive properties
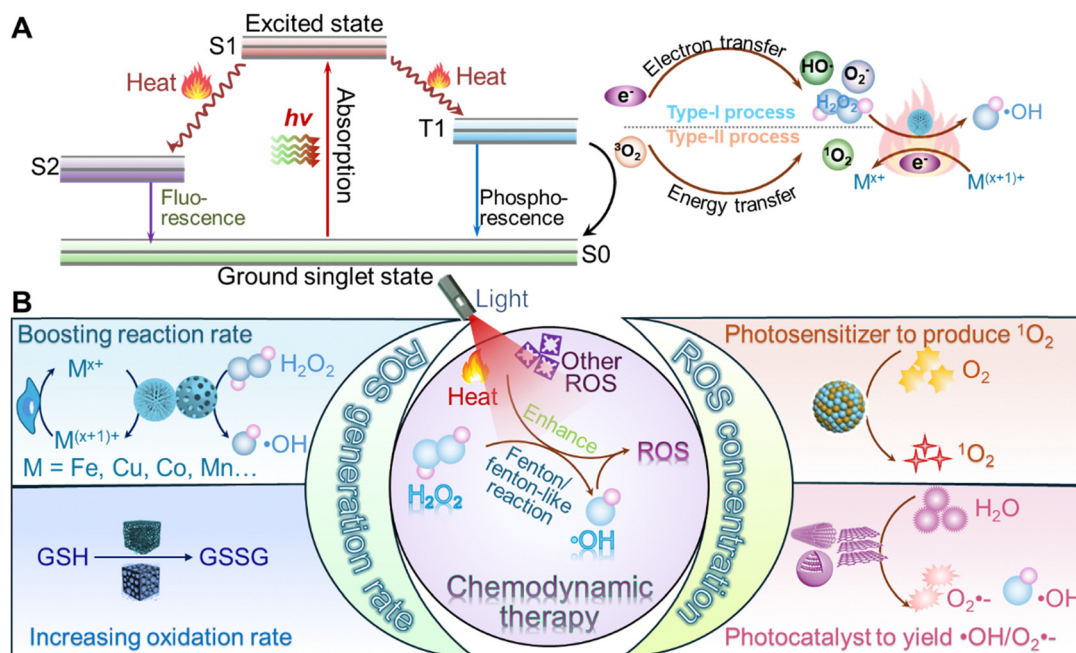
Fig. 2 (A) The mechanistic diagrams for the photothermal-triggered electron transfer pathways, (B) Illustration representing the main mechanism for photo-enhanced CDT from MeSN nanoreactors.

into CDT agents, researchers aim to develop more efficient, targeted, and safe cancer therapies that address the current limitations of conventional treatment modalities.

3. MeSN-based photo-enhanced chemodynamic nNanoreactor for tumor therapy

3.1 Iron sulfide-based nanoreactor

Iron sulfide-based nanomaterials are emerging as a unique class of agents with significant potential for tumor therapy.[36,46,64,65] These materials release Fe^{2+}, which catalyses the conversion of H_2O_2 into highly $^{\bullet}OH$ through the Fenton reaction. The accumulation of $^{\bullet}OH$ induces oxidative stress within tumor cells, ultimately leading to cell death, a process known as CDT. Additionally, iron sulfides exhibit strong NIR absorption, enabling them to generate localized heat for PTT and produce photoinduced electron–hole pairs for PDT. These properties make iron sulfides well-suited for combination therapies, offering a powerful approach to tumor treatment.

Iron, as one of the most abundant elements on Earth and in the human body, makes iron sulfides cost-effective, safe, and biocompatible. The Fe^{2+} released by these nanomaterials can be excreted from the body, reducing the risk of organ retention and minimizing concerns about the accumulation of nanoparticles. These favorable properties make iron sulfides an excellent candidate for tumor therapy. One of the most commonly used iron sulfides for tumor treatment is iron(II) disulfide (FeS_2), also known as pyrite. For example, Bu's group developed pyrite-based PEG (FeS_2-PEG) nanocubes for synergistic PTT and CDT.[31]

Both *in vitro* and *in vivo* studies demonstrated that the localized heat generated from PTT enhanced the CDT effects, leading to reduced tumor size. Similarly, hollow carbon-coated FeS_2 (HPFe$_2$@C) nanocatalysts were designed to improve CDT against tumors under light irradiation.[66] The carbon coating helped convert NIR light into heat, enhancing the PTT effect. The hollow porous carbon structure enhanced the conversion of NIR light into localized heat, boosting the PTT effect. Furthermore, the incorporation of glucose oxidase (GOx) within the nanocatalyst facilitated *in situ* conversion of glucose into H_2O_2, providing more $^{\bullet}OH$ for effective CDT. The reduced glucose in tumor cells also triggered a starvation effect. To target cancer cells specifically, folic acid (FA) was added to the surface of the nanocatalyst.

Recently, Wang and colleagues used carbonic anhydrase inhibitor (CAI) to modify ferrous sulfide nanoparticles (FeS-PEG-CAI NPs) for disrupting the metabolic balance within tumors and enhancing tumor elimination by inducing acidosis (Fig. 3A).[67] The FeS-PEG-CAI NPs were stable under normal physiological conditions and exhibited excellent photothermal properties under 1064 nm-irradiation (Fig. 3B). Under acidic conditions, however, the FeS-PEG-CAI NPs broke down into functional components, including CAI, Fe^{2+}, and H_2S. This degradation triggered the Fenton reaction, where Fe^{2+} catalysed the production of $^{\bullet}OH$ as the pH decreased, enhancing the CDT effect through PTT (Fig. 3C). *In vivo*, the therapeutic potential of the FeS-PEG-CAI NPs was tested in mice. After nanoparticle injection for 8 h, the mice were exposed to laser irradiation. Infrared thermal images showed that the NPs generated localized tumor heat, raising the temperature by 11.27 °C, higher than that in the FeS-PEG group without CAI and acidosis (Fig. 3D). Tumor volume measurements revealed that the FeS-PEG-CAI NPs
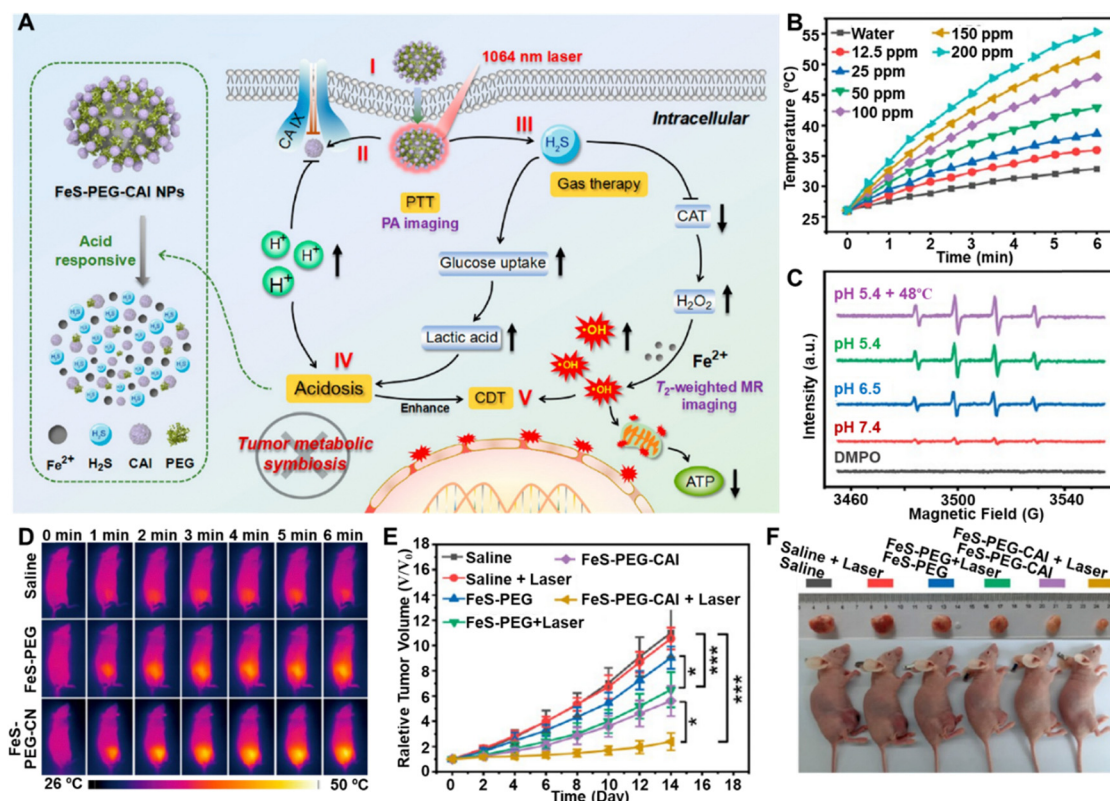
Fig. 3 (A) Graphical representation of FeS-PEG-CAI NPs for the photo-enhanced tumor therapeutic mechanism. (B) Temperature variation in FeS-PEG-CAI NP dispersions at different concentrations irradiated by a 1064 nm laser. (C) Electron spin resonance (ESR) spectra of FeS-PEG-CAI NPs across varied pH and temperature conditions. (D) Infrared thermal imaging of tumor areas with laser irradiation. (E) Tumor volume progression in 4T1 tumor-bearing mice over 14 days. Reprinted with permission from ref. 67. Copyright 2022, Elsevier.

caused the greatest tumor inhibition, demonstrating the synergistic effect of PTT-enhanced CDT (Fig. 3E and F). These findings highlight the potential of FeS-PEG-CAI NPs combined with light-induced PTT for effective tumor therapy.

FeS_2 has a small band gap of 0.96 eV, allowing it to act as a photosensitizer for PDT when activated by an 808-nm laser. This makes FeS_2-based nanomaterials ideal for combined PTT, PDT, and CDT, as they can produce both $O_2^{\bullet-}$ and $^{\bullet}OH$ to destroy tumor cells.[68] To enhance ROS accumulation, FeS_2 NPs can be modified with L-buthionine–sulfoximine (BSO), which blocks GSH synthesis, increasing the effectiveness of the combined therapy. FeS_2-based nanomaterials can also be loaded with chemotherapeutic drugs to improve their therapeutic effectiveness. For instance, sorafenib (SRF) inhibits tumor cell growth and blood vessel formation, boosting ROS accumulation.[69] Paclitaxel (PTX) can also be loaded into these nanomaterials to trigger tumor cell apoptosis. When PTX-loaded nanoreactors (FeS-GOx@PTX) are combined with cytotoxic T-lymphocyte-associated protein 4 (CTLA-4) checkpoint blockade, they promote the infiltration of cytotoxic T lymphocytes (CTLs) into distant tumors, enhancing PTT/CDT/immunotherapy for tumor elimination.[70] Another approach incorporates immunotherapy by loading stimulator of interferon genes (STING) agonists into the nanoreactor. For example, a nanoreactor with the STING agonist cGAMP, FeS_2-BSA, and bromelain can work together

under 1064-nm laser irradiation, enabling PTT-induced CDT and immunotherapy to effectively kill tumor cells.[71] Fe_3S_4 has emerged as a promising iron sulfide for tumor therapy, offering several advantages over FeS_2. Unlike FeS_2, Fe_3S_4 is ferrimagnetic, enabling its use as a magnetic resonance imaging (MRI) contrast agent and for magnetic hyperthermia treatment.[72] Additionally, Fe_3S_4 can be transformed into smaller nanoparticles and Fe ions, which are more easily excreted from the body, making it a safer option for long-term therapy. For instance, Guan and colleagues utilized Fe_3S_4 tetragonal nanosheets for MRI-guided PTT and CDT, achieving complete excretion of the materials from the body.[73] Similarly, Dong's group developed GOx and PEG-modified Fe_3S_4 nanoplates (Fe_3S_4-PEG-GOD),[74] which achieved over 80% shrinkage of both tumors under NIR-II irradiation. These nanocatalysts also provided excellent PAI, further enhancing their therapeutic potential.

3.2 Copper sulfide-based nanoreactors

Copper sulfide-based ($Cu_{2-x}S$, $0 \leq x \leq 1$) nanocatalysts have emerged as promising tools for antitumor therapy and imaging due to their affordability, abundance,[75] simple synthesis, low toxicity, biodegradability, and scalability.[76–78] They feature unique properties, such as LSPR,[79] strong absorption in the NIR region, and high photothermal conversion efficiency (PCE).[80]
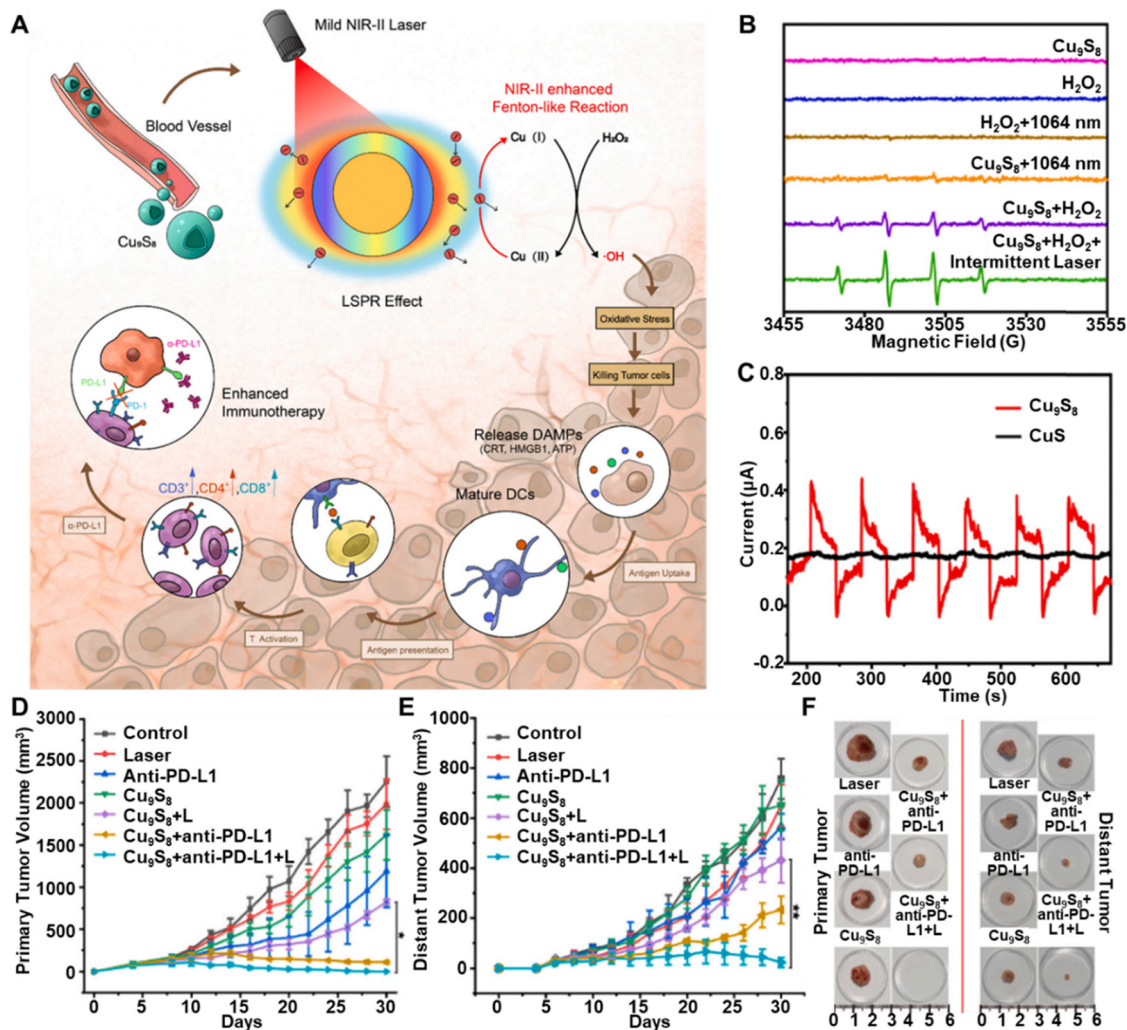
Fig. 4 (A) Diagram showing the mechanism of NIR-II laser-triggered photo-Fenton-like reactions to enhance immunotherapy. (B) The ESR spectrum for different experimental groups. (C) The photocurrent behaviours of Cu_9S_8 nanoparticles and CuS after undergoing six cycles of laser exposure. (D) and (E) The monitoring the primary and distant tumor volume following various treatments. (F) Representative images of tumors following different treatments. Reprinted with permission from ref. 82. Copyright 2022, Elsevier.

Additionally, copper ion d–d orbital transitions ensure stable photothermal performance across various sizes, shapes, and environments.[81]

These properties make $Cu_{2−x}S$ nanocatalysts highly effective in multiple therapeutic applications.[83–87] They serve as contrast agents for PAI and as photothermal agents in PTT. Their ability to generate ROS upon light activation also makes them valuable for PDT.[88] Furthermore, their catalytic versatility extends to Fenton-like reactions,[80] where they outperform iron-based catalysts across different pH levels. Specifically, $Cu_{2−x}S$ reacts with H_2O_2 in the TME to produce cytotoxic •OH, enabling CDT.[79] The superior reactivity of Cu^+ with H_2O_2, compared to Fe^{2+}, and the synergistic heat generation during PTT further enhance CDT efficacy. For example, copper-based metal–organic framework nanoparticles (HKUST-1) were converted into NIR-activated copper sulfide using an H_2S-triggered reaction to improve colon cancer treatment through PTT, CDT, and gas therapy (GT).[89] These combined effects make $Cu_{2−x}S$ nanocatalysts powerful

candidates for multimodal therapies, including PTT, PDT, CDT, and their combinations. Recent advancements in $Cu_{2−x}S$ nanocatalysts have focused on improving treatment outcomes through integrated therapeutic strategies. For instance, although CuS nanoparticles (NPs) have inherent photothermal properties, An et al.[82] developed a Cu_9S_8 NPs platform that operates at room temperature under low-power, short-duration NIR-II laser irradiation, enhancing immunotherapy via plasmon-induced CDT in a photo-Fenton process. As shown in Fig. 4A, self-doped Cu_9S_8 NPs enter the bloodstream and act as efficient Fenton-like agents with strong NIR-II absorption. Mild NIR-II laser irradiation promotes Cu(II)/Cu(I) conversion, boosting ROS generation in the TME, leading to oxidative stress, immunogenic cell death (ICD), and enhanced antitumor immunotherapy. The ESR spectrum in Fig. 4B confirms significantly increased •OH generation under NIR-II laser exposure, indicating enhanced •OH levels through plasmonic effects. Under 1064 nm laser exposure, Cu_9S_8 NPs generate a photocurrent that stops when the laser is turned

off (Fig. 4C), while CuS NPs show no photocurrent, suggesting that Cu_9S_8 NPs rapidly undergo LSPR dephasing, releasing electrons and holes. Fig. 4D and E demonstrate that this synergistic approach significantly ablated primary tumors and inhibited the growth of distant tumors compared to the control group. The enhanced efficacy of anti-PD-L1 therapy *via* NIR-II laser-assisted photo-Fenton-like reactions was further confirmed by a reduction in tumor size for both primary and distant tumors (Fig. 4F), highlighting the significantly enhanced chemodynamic efficiency of Cu_9S_8 NPs with NIR-II irradiation.

Several strategies have been developed for photo-enhanced CDT of targeted and effective anti-tumor therapy. Folic acid (FA), known to target tumors by binding to the folate receptor (FR) overexpressed on many cancer cells, is commonly used in these approaches. Based on this insight, Sun and colleagues functionalized CuS NPs with a FA ligand to selectively target folate receptors on tumor cells.[80] The resulting hybrid system, AIBA@CuS-FA, combines fluorescence imaging-guided PTT, oxygen-independent PDT-like therapy, and CDT, effectively killing cancer cells under low-power NIR-II laser irradiation. Similarly, CuS-based nanostructures functionalized with BSA-FA were developed as a TME-responsive platform for targeted PTT, CDT, and CHT.[90] This platform targets folate receptors on tumor cells, improving drug uptake, stability, and biocompatibility. It integrates CuS NPs with COFs for PTT and CDT, while DOX is loaded into COF mesopores for CHT. Upon NIR irradiation and in the acidic TME, DOX is released, and H_2O_2 levels rise, enhancing CDT. In a unique approach, Liu *et al.*[91] developed a one-pot method to create LDH-CuS nanocomposites (NCs) that localize in cancer cell lysosomes. Under a NIR laser, these NCs increase temperature and release copper ions, generating ROS to enhance CDT. They also promote electron transfer, preventing hole recombination and increasing $^1O_2$ for PDT. The ROS induce lysosomal lipid peroxidation, leading to cell death *via* lysosomal membrane permeabilization. Additionally, a biomimetic nanozyme, CD47@CCM-Lap-CuS NPs, was engineered for combined CDT and PTT in breast cancer treatment.[92] This nanozyme supplies H_2O_2 *in situ* and targets breast cancer cells *via* CD47 overexpression, enhancing targeted therapy efficacy.

Increasing the surface area of copper sulfide-based nanoparticles significantly enhances their catalytic and therapeutic performance. By providing more active sites for H_2O_2 reactions, these nanoparticles boost PTT combined with CDT and support other synergistic treatments. Hollow nanostructures, with their high surface area, have been shown to improve these properties.[93–96] For example, Wang *et al.* developed hollow Cu_9S_8 NPs with 1.7 times the surface area of solid counterparts,[91] improving photothermal properties and chemotherapeutic efficiency. Liu *et al.* coated hollow Cu_9S_8 NPs with PEG and loaded them with DOX, creating DOX@H-Cu_9S_8/PEG nanocomposites that efficiently combine PTT, CHT, and CDT with high drug-loading capacity and NIR-triggered drug release.[97] Building on this, PEGylated pH-responsive peptides (PEG-pHLIP) and lauric acid (LA)-modified hollow CuS nanoparticles (HCuS NPs) were developed for a smart drug delivery system,[98] encapsulating

the stress granule (SG) inhibitor ISRIB to enhance PTT and CDT, effectively inhibiting primary tumors and preventing metastasis. Hu *et al.* applied hollow CuS nanoparticles in a photo-responsive drug delivery platform, D-HCuSHA, combining hyaluronic acid (HA) and losartan for synergistic anti-tumor therapy.[95] Upon laser irradiation, DDTC in CuS reacts with Cu^{2+} to form $Cu(DDTC)_2$, inducing apoptosis and ICD, while losartan enhances T cell infiltration in the TME. For glioblastoma multiforme (GBM), hollow mesoporous copper sulfide nanoparticles (CTHG-Lf NPs) were modified with lactoferrin (Lf), GOx, and HA to improve blood–brain barrier (BBB) permeability and target GBM cells.[99] This modification prevents drug leakage, enabling targeted release and supporting CHT, CDT, PTT, and ST for enhanced treatment.

Porous hybrid platforms, with their high surface areas, are highly effective for enhancing catalytic and therapeutic performance in CDT. For instance, Geng *et al.* developed a copper-based metal–organic framework (Cu-MOF) that incorporates CuS nanodots (NDs) on both the surface and within the pores. This design increases surface area and enables the integration of PTT, CDT, and CHT.[100] The addition of PEG improves dispersibility, while the platform's high DOX loading capacity and responsive drug release in acidic TME further enhance therapeutic outcomes. Similarly, a hybrid nanoplatform combining hierarchically porous porphyrinic coordination networks (HP-PCN) with CuS NPs was developed to enable robust ROS generation for PDT, in addition to CDT and PTT.[101] In another innovative design, Sun *et al.* created SiO$_2$@Cu$_7$S$_4$ nanotubes with dual valency, improving ROS generation and accelerating both CDT and PDT under 808-nm laser irradiation.[102] Additionally, flower-like PS@Cu$_9$S$_8$ nanocatalysts were fabricated using biomineralization strategies, providing a high surface area for enhanced CDT and serving as laser-cavity mirrors for NIR-II light, resulting in high PCE.[103] *In vivo* studies confirmed strong therapeutic efficacy with minimal toxicity. By integrating PTT, CDT, PDT, and CHT, these multimodal platforms enhance antitumor efficacy while minimizing side effects.

Driven by the outstanding performance of nanosheets, ultrathin Cu$_9$S$_5$ nanosheets (NSs) with sulfur vacancies were designed through a one-pot method, enabling multimodal therapies,[104] including PTT, CDT, PDT, and GSH depletion under NIR laser irradiation, as shown in Fig. 5A. Photothermal performance tests demonstrated a positive correlation between Cu$_9$S$_5$ NS concentration and temperature increase under 1064-nm laser exposure (Fig. 5B). With increasing concentration of Cu$_9$S$_5$ NSs, the maximum temperatures were found to increase to 65.9 °C, indicating the good photothermal effect. Additionally, $^1O_2$ production from Cu$_9$S$_5$ NSs was assessed through measuring absorption at 380 nm of 9,10-anthracenediylbis-(methylene) dimalonic acid (ABDA) and H_2O_2 under 1064-nm laser irradiation, confirming efficient $^1O_2$ production for PDT (Fig. 5C). Also, $^•OH$ generation from Cu$_9$S$_5$ NS catalysed H_2O_2 was assessed using terephthalic acid (TAOH). Laser irradiation led to a notable increase in fluorescence intensity at 425 nm, indicating photothermal enhanced CDT (Fig. 5D). *In vivo* antitumor
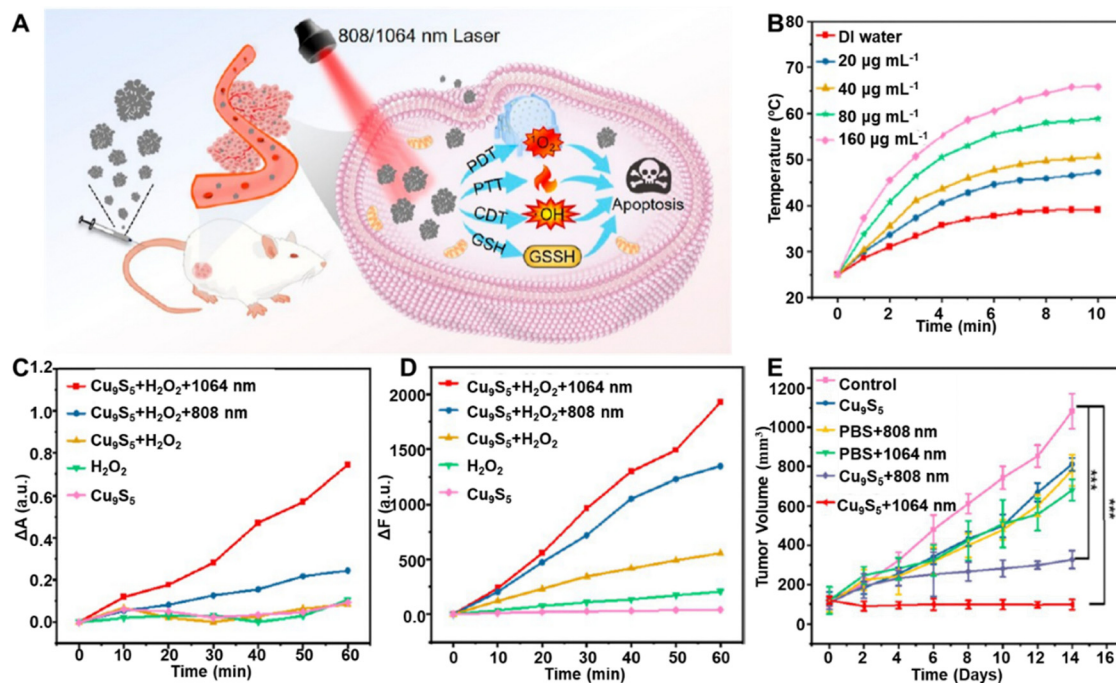
Fig. 5 (A) Diagrammatic representation of Cu_9S_5 NSs for PTT/PDT/CDT under NIR-I and NIR-II irradiation. (B) Temperature evolution of Cu_9S_5 NSs with varying concentrations under a 1064-nm laser. (C) Absorption drop at 380 nm in ABDA solution mediated by Cu_9S_5 NSs and H_2O_2. (D) Reduction of the fluorescence intensity at 425 nm in the TAOH solution facilitated by Cu_9S_5 NSs and H_2O_2. (F) Tumor volume trends under different treatment conditions. Reprinted with permission from ref. 104. Copyright 2024, American Chemical Society.

efficacy was evaluated in a breast cancer mouse model. Tumor growth inhibition was most significant under NIR II laser irradiation (Fig. 5E), highlighting the ability of NIR-II laser irradiation to induce rapid temperature increases, $^1O_2$ and $^\bullet OH$ production, triggering apoptosis through PTT, PDT, and CDT.

A critical limitation of CDT is the insufficient concentration of H_2O_2 in tumors, which restricts its ability to eliminate cancer cells resistant to oxidative stress. To address this challenge, researchers have developed strategies for *in situ* H_2O_2 generation, primarily using GOx. GOx catalyses the oxidation of glucose into gluconic acid and H_2O_2, simultaneously depleting glucose to starve tumor cells and sustaining $^\bullet OH$ production to enhance CDT efficacy. In a paradigm, Kong *et al.*[105] developed a biomimetic enzyme system, CuS/G5-GOx, designed for pH-responsive CDT and enhanced PTT. A Generation 5 poly(amidoamine) (G5) dendrimer protected GOx until tumor-specific release, effectively preventing breast cancer recurrence and metastasis under laser irradiation. Similarly, Singh *et al.*[81] synthesized GOx-coated CuS nanocomposites (GOx@CuS) integrating PTT, PDT, ST, and chloride-accelerated CDT under NIR irradiation. The presence of chloride ions enhanced Cu-based CDT (Cl-Cu CDT), boosting ROS production. Within glucose- and chloride-rich tumors, GOx@CuS formed a nano-cascade system that regenerated H_2O_2, achieving effective tumor eradication. Another promising approach involves mesoporous $Cu_{2-x}S$ NPs (HMCu$_{2-x}$S) functionalized with GOx and oxygen-loaded perfluoropentane (PFP) (PO@HMCG).[88] Upon NIR irradiation, PFP transitioned to gas, releasing oxygen to sustain ROS generation, which demonstrated strong antitumor effects without toxicity *in vivo*.

A delivery patch offers a promising site-specific approach for cancer treatment.[106] For instance, a thermosensitive hydrogel co-loaded with CuS NPs and camptothecin (CPT) can induce apoptosis while activating nicotinamide adenine dinucleotide phosphate oxidase (NOX) to generate H_2O_2. The heat generated by CuS NPs enhances CDT, while CPT further amplifies CDT efficacy by blocking DNA synthesis.[107] To endow the benefits of the patch to photothermal enhanced CDT combining with GOx, researchers have developed various patches, including microneedles (MNs), hydrogels, and membranes, designed to penetrate the skin's outer layer for efficient GOx and CuS NP delivery.[108] For instance, a dissolvable MN loaded with GOx-CuS NCs utilizes tumor glucose to generate H_2O_2, synergizing ST, PTT, and CDT for melanoma treatment.[109] An innovative bubble pump microneedle system (BPMN-CuS/DOX) was developed for transdermal cancer therapy, integrating CDT, PTT, and CHT.[110] Encapsulated $NaHCO_3$ generates CO_2 in the acidic TME, enhancing drug penetration and controlled DOX release. Additionally, fucoidan coating improves biocompatibility and immune regulation, while CuS NPs facilitate PTT and CDT. DOX further increases H_2O_2 levels, amplifying CDT efficacy.

Another strategy for developing nanoplatforms for antitumor treatment involves using a polymeric matrix to encapsulate CuS NPs and other active agents, enabling controlled release in response to PTT-generated heat. For example, Ning and coworkers co-loaded hollow CuS NPs and β-lapachone (Lap) into agarose hydrogels, facilitating a self-sustaining H_2O_2 supply to enhance CDT efficacy.[111] Various researchers have employed this approach to integrate PTT with enhanced CDT by

ensuring a self-sustaining supply of H_2O_2. For instance, Wu et al.[112] designed a thermos-responsive liposome shell loaded with CuS NPs and GOx, enabling controlled H_2O_2 production. More recently, He et al. developed AG@Cu_9S_8@dOMV NPs,[113] which were camouflaged with lipopolysaccharide-free bacterial outer membrane vesicles (dOMV) to improve BBB penetration and GBM targeting. These nanoparticles, loaded with AQ4N and GOx, consumed glucose and oxygen, inducing ST, generating H_2O_2 for CDT, and activating AQ4N under hypoxic conditions. Upon NIR-II irradiation, Cu_9S_8 enhanced CDT efficacy and drug release. In vivo studies demonstrated significant GBM inhibition without increasing heat shock protein (HSP) expression.

In conclusion, CuS NPs show great potential for cancer treatment by integrating PTT, CDT, and PDT. To enhance their efficacy, CuS NPs can be loaded with anticancer drugs such as DOX for CHT, as well as GOx, which not only facilitates the in situ generation of H_2O_2 to enhance CDT but also achieves ST via glucose consumption. Furthermore, CuS NPs can be tailored for specific tumor targeting by adding ligands such as FA. Studies have demonstrated that CuS nanoplatforms effectively inhibit primary tumors and help prevent metastasis with minimal toxicity.

3.3 Cobalt sulfide-based nanoreactors

Beyond the commonly used transition metal ions in CDT, cobalt has emerged as a promising candidate, particularly in the form of cobalt complexes. Recent studies have highlighted the potential of cobalt-based nanomaterials in enhancing ROS generation, thereby improving tumor targeting and therapeutic efficacy.[114] As an exemplary work, monodispersed CoS_2 nanoclusters were developed using the La Mer scheme to achieve a synergistic PTT/CDT approach.[115] These nanoclusters exhibited excellent PCE and catalytic activity for Fenton-like reactions, significantly enhancing cancer cell eradication in both in vitro and in vivo models while maintaining biodegradability and low toxicity. A key feature of Wang's work was the defect-engineered, loosely stacked CoS_2 nanocrystals, which increased catalytic sites for converting endogenous H_2O_2 into cytotoxic •OH while enabling oxidation into smaller, excretable species via the reticuloendothelial system. Building on this, Zhao et al. synthesized two-dimensional cobalt chalcogenide nanodots ($Co_{2.19}S_2$ NDs) through a one-step solvothermal method, demonstrating potent ST properties.[116] With strong optical absorption, efficient photothermal conversion, and rapid degradation into Co^{2+} and S^{2-}, these NDs synergistically enhanced CDT and PTT. Their study demonstrated effective tumor suppression through ST and PTT-enhanced CDT, achieving significant antitumor efficacy.

Leveraging the exceptional Fenton-like performance of CoS nanomaterials, Zhu et al. developed sulfur-deficient biodegradable cobalt sulfide quantum dots (CoS_x QDs) to enhance cancer therapy.[117] These QDs induce cancer cell death through four key mechanisms (Fig. 6A): (1) Fenton-like reaction, (2) GSH depletion, (3) PTT, and (4) PTT-enhanced Fenton-like reaction. The defect-engineered CoS_x QDs catalyse endogenous H_2O_2 into ROS, causing oxidative damage while oxidizing GSH to GSSG, further amplifying ROS production by disrupting cellular

antioxidant defences. Their strong photothermal properties enable direct cancer cell ablation, with heat further accelerating the Fenton-like reaction and ROS generation. The photothermal effect of CoS_x QDs was concentration-dependent, with a significant temperature increase observed within five minutes (Fig. 6B). ESR spectra confirmed enhanced Fenton-like activity at higher temperatures (pH 6.5, 40 °C), indicating increased ROS production and accelerated CDT (Fig. 6C). In vivo, tumor temperatures in mice injected with CoS_x QDs rapidly rose to 52 °C, demonstrating effective hyperthermia-induced tumor inhibition (Fig. 6D). While CoS_x QDs exhibited strong •OH generation in the TME, the Fenton-like reaction alone was insufficient for complete tumor eradication (Fig. 6E and F). However, this demonstrated that their biodegradable CoS_x QDs significantly enhanced CDT and PTT efficacy, leading to complete tumor suppression under NIR irradiation.

Given the limitations of single-modality therapies, researchers have increasingly adopted multi-modal approaches to improve tumor ablation. For instance, Jiang et al. developed a trimodal PDT/PTT/CDT strategy, effectively enhancing therapeutic efficacy through a synergistic "kill three birds with one stone" approach.[118] They incorporated the photosensitizer indocyanine green (ICG) into hollow Co_3S_4 NPs, which degrade in the acidic TME to release Co^{2+}, triggering a localized Fenton-like reaction and generating cytotoxic •OH for CDT. The Co_3S_4-ICG nanocomplex exhibited superior therapeutic potential, efficiently producing $^1O_2$ for PDT and achieving a high PCE (40.5%), enabling simultaneous PDT and PTT under laser irradiation, ultimately leading to effective tumor ablation. Further advancing this multi-modal paradigm, GOx-encapsulated mesoporous hollow Co_9S_8 nanoreactors were designed to coat with polyphenol block copolymers (POEGMA-b-PDOPA) to enhance tumor ablation.[119] Their GOx@PCoS nanoreactors, exhibiting superior PCE (45.06%), facilitated potent phototherapy and oxygen generation under NIR laser irradiation. To maximize therapeutic efficacy, they developed a multifunctional cascade nanoreactor integrating CDT, GSH depletion, PDT, ST, and PTT. These studies underscore the potential of multi-modal strategies in improving antitumor efficacy and advancing cancer treatment.

3.4 Other unitary metal sulfide-based nanoreactors

Beyond copper, cobalt, and iron sulfide-based materials, other binary metal sulfides have also gained attention as promising candidates for photo-enhanced CDT nanotheranostics in tumor treatment. These nanomaterials leverage the unique properties of transition metal sulfides, such as their excellent PCE, redox activity, and ability to catalyse the decomposition of H_2O_2 into ROS. When exposed to NIR light, these nanomaterials generate localized heat, enhancing their CDT efficiency by accelerating Fenton-like reactions and promoting oxidative stress within tumor cells. Additionally, their tunable band structures enable synergistic interactions with PDT and PTT, further amplifying their antitumor effects. Recent studies have demonstrated that binary metal sulfides, including manganese sulfide (MnS), molybdenum oxo-sulfide (Mo_xS_{2-x}),[35,120,121]
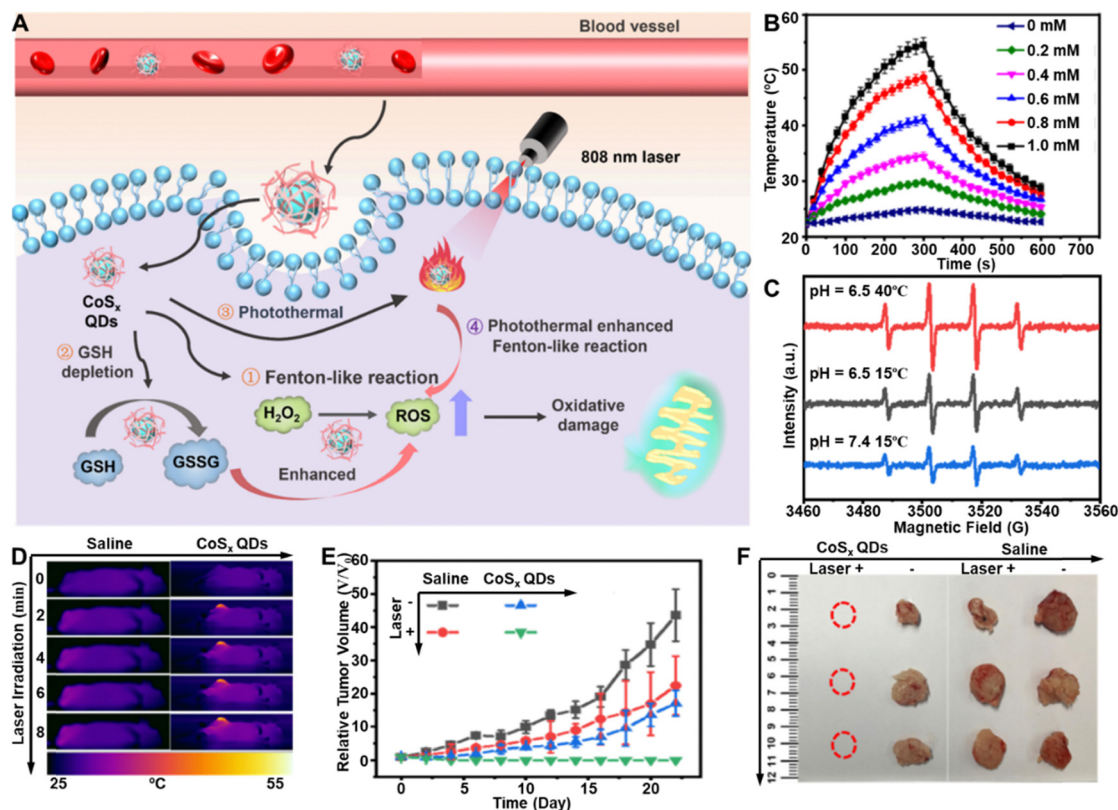
Fig. 6   (A) Graphical representation of biodegradable CoS$_x$ QDs for photothermal and heat-enhanced CDT of tumors. (B) Relevant photothermal heating profiles of CoS$_x$ QDs at varying concentrations under 808-nm laser irradiation. (C) ESR spectra of 5,5-dimethyl-1-pyrroline-N-oxide (DMPO) capturing •OH under diverse conditions. (D) IR images of tumor-bearing mice following laser irradiation after intravenous administration of saline or CoS$_x$ QDs. (E) Tumor growth progression in various mouse groups. (F) Digital images of surgically removed tumors. Reprinted with permission from ref. 117. Copyright 2022, American Chemical Society.

bismuth sulfide (Bi$_2$S$_3$), and silver sulfide (Ag$_2$S), exhibit significant potential in tumor theranostics, offering multimodal imaging capabilities, controlled drug release, and targeted therapeutic effects.

To further enhance anticancer efficacy, doping with manganese (Mn) has been explored to boost free electron flow and activate both radical and non-radical pathways for catalytic degradation. The release of Mn^{2+} also enables MRI and Mn-based CDT.[58,122,123] Within this context, one notable example is MnS nanocomposites. Ma *et al.* demonstrated the effectiveness of a PDA-coated MnS nanocluster as both a contrast agent for MRI and a nanoplatform for synergistic ferroptosis-photothermal therapy (Fig. 7A).[124] The MnS@PDA nanoplatform was created by coating spherical MnS with PDA, enhancing the interaction between the pH-sensitive MnS and water molecules through hydrogen bonding. This interaction improved tumor MRI efficiency, with the spin–lattice relaxation time increasing from 5.76 mM^{-1} s^{-1} for unmodified MnS to 19.33 mM^{-1} s^{-1} for the nanocomposite at pH 5.5. MnS@PDA also exhibited notable photothermal properties, with temperature rising in proportion to nanocomposite concentration (Fig. 7B). The combination of PTT and MnS-mediated effects significantly enhanced antitumor activity. In the acidic TME, MnS releases hydrogen sulfide (H$_2$S), sensitizing tumor cells

to PTT by inhibiting mitochondrial respiration and ATP production, which reduces heat shock protein levels. Additionally, released Mn^{2+} exhibits potent peroxide (POD) and glutathione oxidase (GSHox) activities, converting abundant H$_2$O$_2$ into highly reactive •OH, depleting GSH, and inducing synergistic ferroptosis and apoptosis through catalytic cell death, further amplified by photothermal effects (Fig. 7C). *In vivo* studies confirmed the remarkable antitumor efficacy of MnS@PDA, achieving complete tumor volume inhibition under NIR irradiation (Fig. 7D).

Except for the aforementioned MeSNs, a NIR-responsive Bi$_2$S$_3$@Bi Z-scheme heterostructure was developed for synergistic PTT, CDT, and PDT in hypoxic tumors.[125] Hydrazine post-treatment of solvothermally synthesized Bi$_2$S$_3$ nanorods induced the formation of a Bi-layer, enhancing both PTT and PDT efficacy. Additionally, coating with PDA/ammonium bicarbonate (PDA/ABC) and HA enabled targeted artesunate (Art) delivery. Art-mediated transferrin degradation elevated intracellular Fe^{2+} levels, promoting ROS generation for efficient CDT. Furthermore, Ag$_2$S NPs have emerged as an attractive therapeutic platform.[126,127] Bio-responsive Janus nanoparticles (JNPs) based on Ag$_2$S were designed for precise NIR-II bioimaging and tumor therapy.[128] The asymmetric Ag$_2$S-sulfur heterostructure, coated with polyethylene glycol (PEG), facilitated
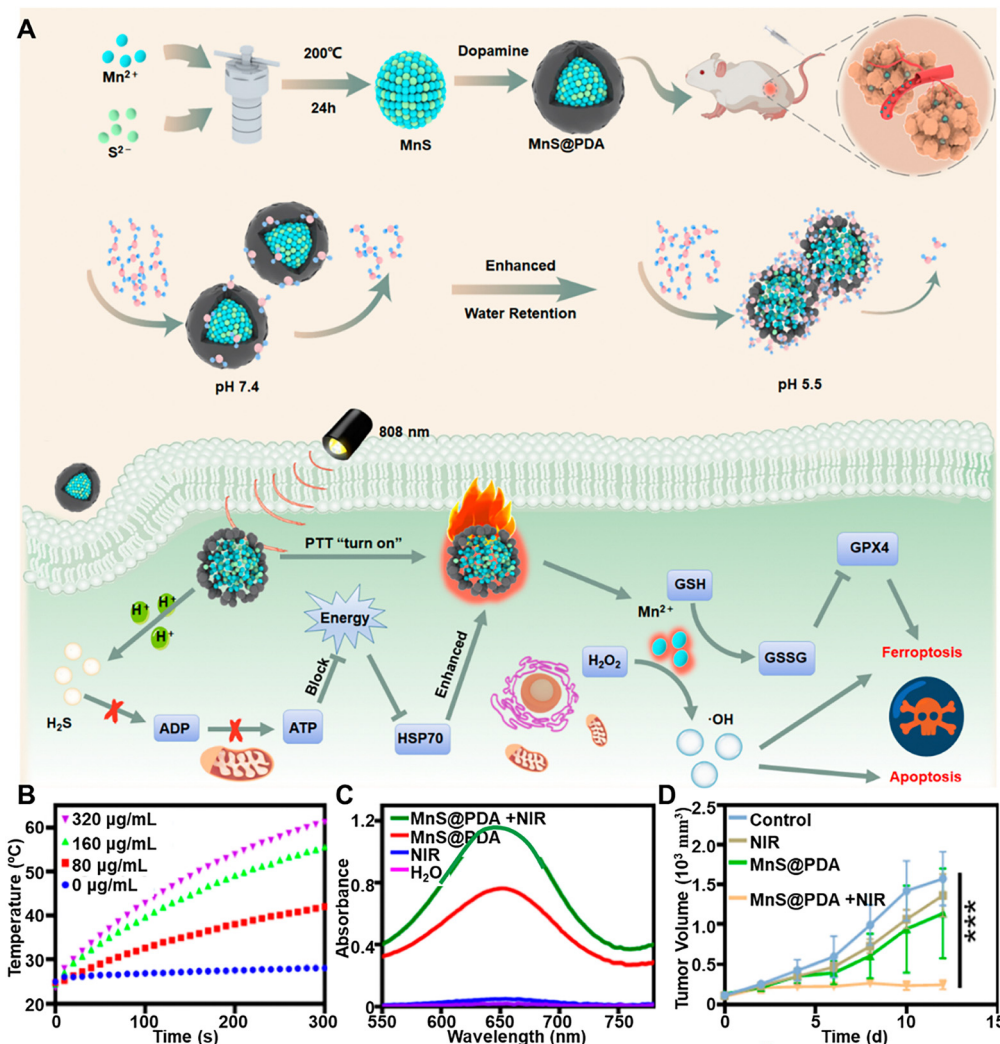
Fig. 7 (A) Diagram depicting the MnS@PDA synthesis process, the role of the PDA shell in modulating water molecule interactions across different pH levels, and the underlying mechanisms by which MnS@PDA enhances PTT and ferroptosis-based tumor treatment. (B) Temperature variations of MnS@PDA at varying concentrations under photothermal irradiation. (C) UV-vis absorption spectra of TMB in the presence of H_2O_2, comparing conditions with and without NIR irradiation. (D) Tumor growth trends following different treatment regimens. Reprinted with permission from ref. 124. Copyright 2024, American Chemical Society.

dual-mode treatment. Ag_2S JNPs exhibited strong PTT capability, while silver (Ag) catalyzed the decomposition of H_2O_2 into highly reactive •OH, enhancing CDT. The Janus structure further amplified CDT effects, achieving a high PCE of 56.8%. These JNPs demonstrated potent antitumor efficacy, resulting in a tumor inhibition rate of 96.2% through PTT-enhanced CDT.

3.5 Binary metal sulfide-based nanoreactors

Building on the use of MeSNs in photo-enhanced Fenton/Fenton-like tumor therapy, binary structures have been developed to enhance PCE, ROS generation, and advanced imaging capabilities compared to individual metal sulfides. These complex formations offer improved stability, biocompatibility, and multifunctionality by integrating multiple therapeutic modalities such as PTT and CDT.[129,130] This subsection highlights the advantages of binary and ternary metal sulfides over their individual counterparts, particularly in terms of high PCE,

enhanced ROS generation, advanced imaging capabilities, and synergistic therapeutic effects. These benefits underscore their potential as superior alternatives for targeted tumor therapy.

3.5.1 Enhanced photothermal conversion efficiency (PCE). Binary metal sulfides are widely adopted in photo-enhanced Fenton/Fenton-like tumor therapy due to their high PCE and sustained photothermal stability. These nanoreactors efficiently convert NIR light into heat, inducing hyperthermia for tumor ablation, while also facilitating enzyme-like activities that generate ROS. This dual mechanism exerts oxidative stress on cancer cells, significantly enhancing therapeutic outcomes.[126]

Several strategies have been employed to improve their NIR absorption capabilities. A prominent approach is leveraging the LSPR effect, which enhances the photothermal properties of ternary Cu_5FeS_4 NPs.[131] This strategy enables Cu_5FeS_4 NPs to achieve a PCE of 45.9%, substantially surpassing unitary counterparts such as $CuFeS_2$ (36.6%) and FeS_2 (24.4%). The improvement

arises from modulating the LSPR characteristic peak shift toward longer wavelengths by increasing Cu/Fe ratios. Doping metals into CuS NPs with inherent photothermal properties has been shown to enhance chemodynamic antitumor efficacy. In one design,[132] Mn-doped Cu_7S_4 nanospheres (Cu(Mn)S) exhibited high PCE (40.3% NIR-I, 33.4% NIR-II), enabling PTT, CDT, and CHT for effectively inhibiting tumor growth *in vivo*. Through a similar approach, doping Ag into CuS (BSA-Ag:CuS NPs) achieves a 37.8% of PCE for enhanced PTT and CDT of halted tumors.[133]

Other binary systems have demonstrated improved photothermal properties through compositional, surface, and morphological modifications. For instance, Cu integration in $Co_{3-x}Cu_xS_4$ nanoparticles enhances NIR absorption without compromising their crystalline structure.[134] Similarly, surface decoration of Fe on BiNS in BiNS-Fe@Fe enhances the SPR effect and introduces deep-level defects, generating additional electrons to improve optical absorption and photothermal efficiency.[135] Hollow core–shell structures, such as Mn–CoS@C and $CoSnS_2$, utilize multiple reflections of incident light within the hollow structure to achieve notable improvements in PCE and stability.[136,137] The advantages of binary metal sulfides over unitary counterparts are exemplified by MoS_2/Co_3S_4@PEG nanoflowers, which exhibit a PCE of 39.4% under a 1064 nm laser compared to 33.2% for MoS_2@PEG.[138] Similarly, PEGylated $Co_{3-x}Cu_xS_4$ achieves a PCE of 46.7% under an 808-nm laser, far exceeding the 33.1% observed for Co_3S_4.[134] These examples underscore the robust PTT functionalities of binary metal sulfide-based nanoreactors.

3.5.2 Enhanced ROS generation.
Binary metal sulfides significantly enhance ROS generation compared to their individual metal sulfide counterparts by exploiting synergistic interactions between their constituent metals. This enhancement occurs through both photocatalytic and Fenton-like reaction pathways. Effective charge separation is a critical factor in photocatalytic ROS generation and can be achieved by constructing Z-scheme heterojunctions within these materials. Such configurations reduce charge recombination rates and increase the efficiency of photocatalytic processes.[138–140] For example, Z-scheme mechanisms in FeS_2/CoS_2@PEG and MoS_2/Co_3S_4@PEG enhance charge separation and improve ROS production.[138,139] Schottky-type heterostructures, such as iron-doped bismuth-core–shell heterostructures, further optimize the band gap through Fe doping and charge redistribution. This creates a strong electron cloud near the Bi atom, preventing charge recombination and boosting ROS generation.[135] Additionally, core–shell interactions in binary metals facilitate enhanced redox cycling and charge separation. For instance, doping Mn into Mn–CoS@C dishells introduces new energy bands, improving redox cycling and enabling sustained ROS production.[136] These advancements demonstrate the potential of binary metal sulfides as powerful nanoreactors for tumor therapy, combining enhanced photothermal efficiency with superior ROS generation to achieve synergistic therapeutic outcomes.

In Fenton-like reactions, binary metal sulfides leverage multivalent redox cycles to enhance catalytic efficiency. Elements such as Cu, Mo, Co, and Sn can transition between multiple oxidation states, continuously regenerating active catalytic species and sustaining high levels of ROS production.[141–146] For instance, the Cu^+/Cu^{2+} and Mo^{4+}/Mo^{6+} redox pairs in materials like Mo–Cu_9S_5 enable dynamic cycling, which boosts Cu^+ generation and enhances Fenton-like reactions.[142] The photothermal effect in PTT further accelerates these reactions, as elevated temperatures increase reaction rates and improve ROS generation, as demonstrated in studies on Cu_5FeS_4 and CuS/Gd_2O_3, which highlight the temperature-dependent efficiency of Fenton-like reactions.[131,147] To overcome limitations in Fenton-like reactions, innovative strategies have been developed. These include the design of pH-independent catalysts like $CuFeS_2$ for synergistic CDT-PDT tumor therapy[148] and the use of prodrug systems, such as CuS–Fe@polymer, to ensure a sustained release of Fe^{2+} for prolonged Fenton activity.[149] Another effective approach is GSH depletion in cancer cells, which prevents the scavenging of generated •OH. For example, $Co_{3-x}Cu_xS_4$ and BSA-(Bi^{3+}/Cu^{2+})-DATS nanoreactors combine GSH depletion with redox cycling to maximize ROS generation and Fenton-like reaction efficiency.[134,150]

By integrating these strategies, binary metal sulfides significantly improve the catalytic performance and amplify therapeutic effects in photo-enhanced Fenton/Fenton-like tumor therapy, establishing them as highly effective alternatives to individual metal sulfides.

3.5.3 Synergistic therapeutic modalities.
Combining multiple therapeutic modalities is crucial for achieving synergistic effects in tumor therapy, minimizing invasiveness and side effects while enhancing curative outcomes. For example, Ruan *et al.* synthesized polydopamine-coated $Zn_xMn_{1-x}S$ hollow nanospheres (ZMS@PDA) with tunable shell thickness determined by the Zn/Mn ratios, enabling effective synergistic PTT and CDT (Fig. 8A).[129] The nanocomposites demonstrated an impressive PCE of 32.79% under laser irradiation, with temperature increases from 25 °C to 53.6 °C, depending on the PDA mass ratio and laser intensity (Fig. 8B). Using methylene blue (MB) as a probe molecule, ZMS@PDA was confirmed as an effective Fenton-like agent, producing •OH that degraded MB (Fig. 8C). Subsequent *in vitro* studies with cancer cells confirmed its cytotoxicity, while *in vivo* experiments on 4T1 tumor-bearing mice further validated the biocompatibility and therapeutic efficacy of ZMS@PDA in tumor treatment (Fig. 8D–F). The results revealed significant tumor volume reduction and effective tumor growth inhibition through the combined PTT and CDT effects. The antitumor efficacy of ZMS@PDA was attributed to its ability to deplete intracellular GSH, thereby reducing the oxidative resistance of cancer cells and enhancing the CDT effect. Photothermal treatment amplified the catalytic efficiency of the Fenton-like reaction, leading to increased ROS production and subsequent cancer cell apoptosis. The synergistic PTT and CDT effects demonstrated by ZMS@PDA highlight its potential as a multifunctional platform for cancer therapy.

Similar synergistic effects of PTT and CDT have been observed in other studies, including those involving $MoS_2/FeGA$,[144] $BSA-CuFeS_2$,[148] and Cu_2ZnSnS_4@BSA (CZTS@BSA),[151] which also achieved enhanced tumor elimination and growth inhibition through combined therapeutic modalities.
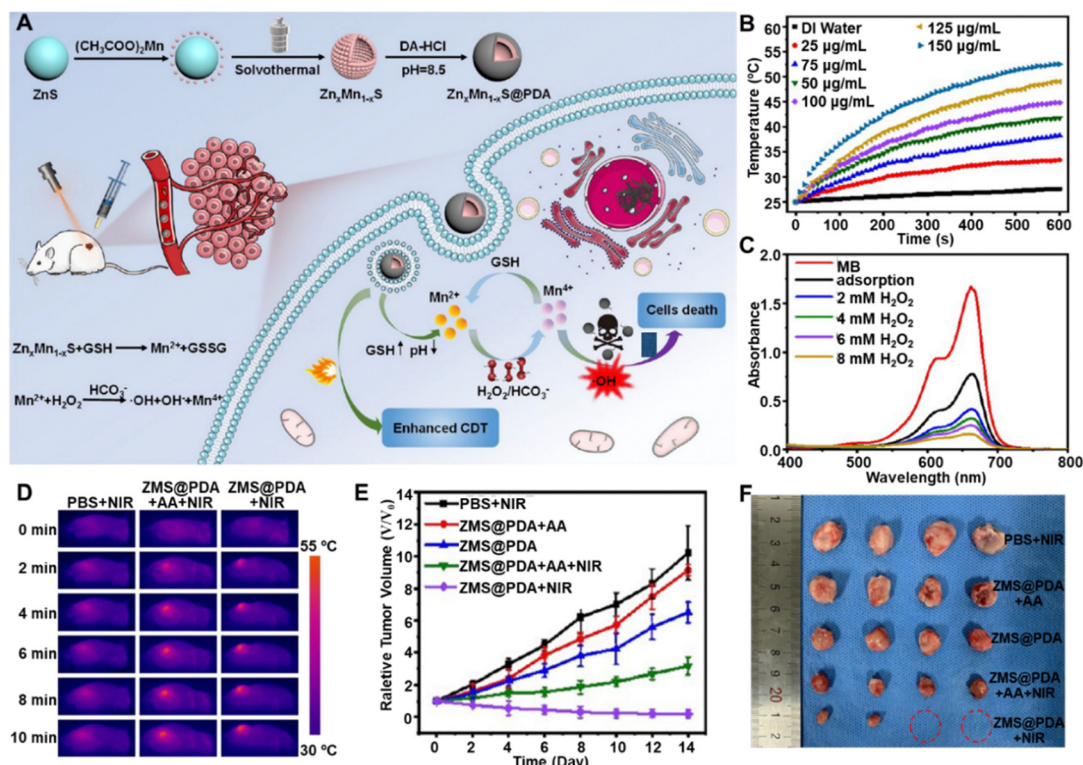
Fig. 8 (A) Illustrative depiction of the synthesis and structural design of ZMS@PDA hollow nanospheres for enhanced synergistic PTT/PDT of cancer. (B) Heat variation in ZMS@PDA suspensions under NIR laser stimulation. (C) MB decomposition following exposure to varying concentrations of H_2O_2. (D) Thermal infrared visualization across different treatment groups. (E) Normalized tumor growth trajectories. (F) Images of excised tumors from various treatment groups. Reprinted with permission from ref. 129. Copyright 2021, American Chemical Society.

3.5.4 Enhanced imaging capabilities. Binary metal sulfide nanoreactors also exhibit enhanced imaging capabilities, enabling precise tumor localization and monitoring during therapy. The photothermal effect of these nanoreactors generates a temperature gradient, facilitating IR imaging visualization. The strong NIR absorption properties of ultrasmall CZTS@BSA and $Cu_xMn_yS_z$ nanoreactors provide excellent PA contrast, making them effective for PAI.[142,151] Furthermore, these nanoreactors exhibit high longitudinal relaxivity, which enhances their performance as T_1-weighted MRI contrast agents.

Nanoreactors capable of attenuating X-rays can also serve as efficient CT imaging agents. Studies involving Bi_2S_3@Fe/Mn-ZIF-8, BSA-CuS/Gd_2O_3 NPs, BiNS-Fe@Fe and Mn–CoS@C highlight trimodal imaging capabilities, including CT imaging.[135,136,147,152] For example, the bismuth in BiNS-Fe@Fe, a high atomic number element, enables superior X-ray attenuation for CT imaging, while magnetic Fe ions contribute to MRI, and robust NIR absorption facilitates PAI. Similarly, Lv *et al.* demonstrated the efficacy of their bimetallic chalcogenides as CT contrast agents, offering integrated MRI/CT/photothermal imaging functionality.

To improve tumor-specific therapeutic efficacy while minimizing adverse effects, Zhu *et al.* developed a poly(L-lysine) (PLL)-encapsulated, tirapazamine (TPZ)-loaded, Cu-doped SnS_2 nanosphere (TPZ@Cu-SnS_{2-x}/PLL) for enhanced tumor-specific therapy with minimal side effects (Fig. 9A).[130] Copper doping and sulfur vacancies were introduced into Cu–SnS_{2-x} nanospheres using a sacrificial template method, improving their photothermal and catalytic properties. This modification resulted in a temperature increase of up to 27.5 °C and a PCE of 32.8% (Fig. 9B). The Cu doping enhanced NIR absorption and carrier separation, optimizing the material for PTT. The hollow nanostructure provided high stability and a drug loading capacity of 93% for TPZ, with PLL enabling pH- and temperature-responsive release. TPZ release was significantly enhanced in the acidic TME and elevated temperatures from PTT, improving therapeutic efficacy. This intelligent nanoplatform combines PTT and CHT for synergistic tumor treatment with minimal off-target effects. *In vitro*, Cu–SnS_{2-x}/PLL nanocomposites exhibited excellent catalytic activity, generating •OH from H_2O_2 due to Cu ions (Fig. 9C). The presence of GSH further enhanced the catalytic activity by converting Cu^{2+} to Cu^+, promoting ROS generation. Sulfur vacancies also facilitated charge separation, increasing PDT efficacy by preventing carrier recombination. Further studies confirmed enhanced cytotoxicity under NIR irradiation, leading to significant apoptosis in cancer cells. *In vivo*, nanocomposite accumulation in tumor tissues was monitored *via* dual-modality imaging: NIR absorption enabled PAI, and Sn's high X-ray attenuation allowed CT imaging for precise, real-time therapy monitoring. The combined effects of ROS generation, GSH depletion, and
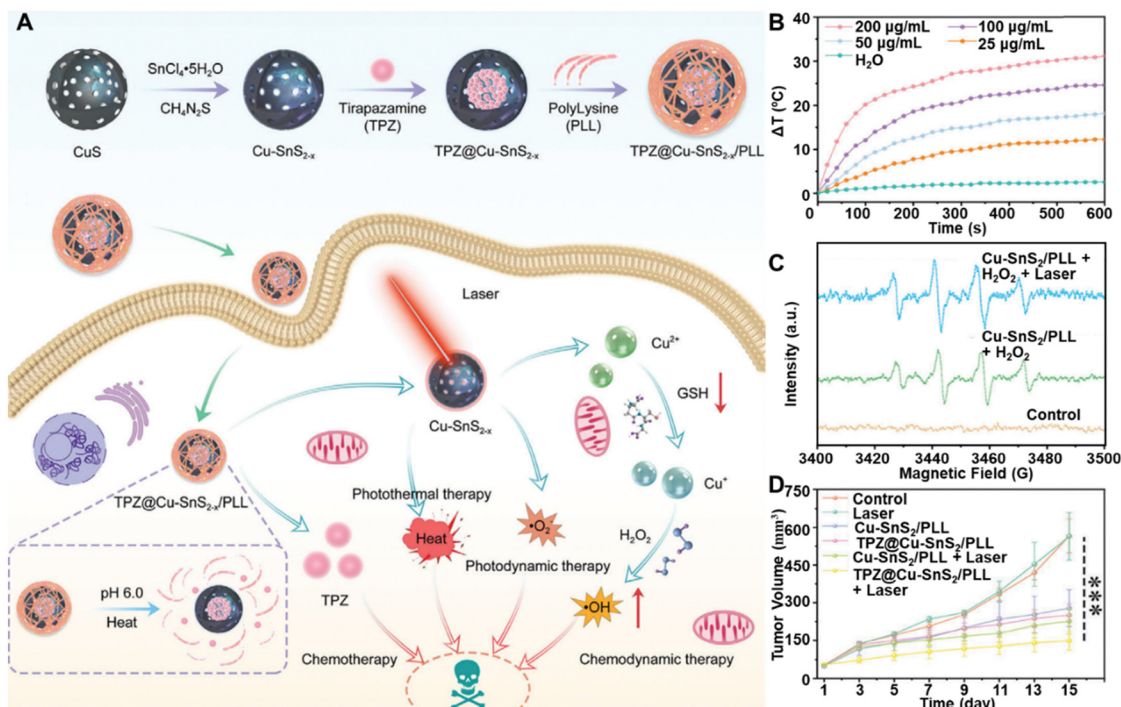
Fig. 9 (A) Schematic representation of the synthesis process of TPZ@Cu−SnS$_{2-x}$/PLL nanocomposites and their underlying mechanism in facilitating synergistic cancer therapy. (B) Laser-induced temperature changes in TPZ@Cu-SnS$_{2-x}$/PLL at varying concentrations. (C) ESR analysis of •OH production following different treatments. (D) Tumor volumes in mice subjected to various treatments. Reprinted with permission from ref. 130. Copyright 2024, Wiley.

controlled drug release induced oxidative stress, mitochondrial damage, and apoptosis without systemic toxicity (Fig. 9D). The strategic incorporation of copper ions, sulfur vacancies, and multimodal imaging guidance enhanced therapeutic outcomes, integrating PDT, PTT, CDT, and CHT into a unified tumor treatment platform.

In a similar vein, Wu *et al.* developed biodegradable doxorubicin-loaded Fe(III) species-WS$_2$-polyvinylpyrrolidone (DOX@Fe(III)@WS$_2$-PVP) nanocapsules for combined PTT/CDT/CHT.[153] Other studies have also successfully combined multiple therapies to create multifunctional nanotheranostic platforms. Examples include Cu$_2$MoS$_4$/GOx for CDT/PTT/ST/immunotherapy,[141] and pH-responsive supramolecular hydrogels encapsulating CuMnS$_2$ and TiO$_{2-x}$@Cu,S-MONs@GOx for PTT/CDT/GT/ST.[154,155]

In summary, the application of binary and ternary MeSNs in photo-enhanced Fenton/Fenton-like tumor therapy has led to significant advancements in PCE, ROS generation, and imaging capabilities. These multifunctional nanostructures offer improved stability, biocompatibility, and therapeutic efficacy. Key strategies, such as LSPR effects, compositional modifications, and core–shell configurations, have been instrumental in enhancing these properties. By integrating multiple therapeutic modalities, including PTT and CDT, these nanoplatforms achieve synergistic effects that minimize invasiveness and side effects while maximizing antitumor efficacy. The inclusion of advanced imaging capabilities ensures precise tumor localization and monitoring, supporting effective diagnosis and

treatment planning. These innovations underscore the potential of metal sulfide nanoreactors as transformative tools for targeted tumor therapy.

4. Conclusions and future prospects

As a catalysis-driven approach toward cancer treatment, CDT has attracted considerable attention for its ability to selectively target tumors by exploiting their unique microenvironment. Particularly promising are CDT-based combinatorial systems that incorporate photo-activation, which have emerged as highly encouraging strategies for cancer theranostics. These systems synergistically combine the advantages of CDT with photo-responsive modalities, such as PTT or PDT, to achieve precise tumor targeting and enhanced therapeutic efficacy. Photo-activation not only amplifies ROS production from nanoagents, but also presents spatiotemporal control over treatment, minimized off-target effects and improved safety profiles. The integration of photo-activated systems with CDT enhances the versatility of cancer theranostics and has great potential for achieving robust therapeutic outcomes, offering a pathway to more effective and personalized cancer treatments.

In this review, we have provided an overview of the typical Fenton MeSNs and their photo-enhanced catalytic mechanisms, highlighting their ability to improve the efficiency of CDT through synergistic photoactivation. Additionally, we have summarized the recent advancements in the design and

application of MeSNs for photo-enhanced CDT, emphasizing their potential to revolutionize cancer treatment by combining precise tumor targeting with robust therapeutic outcomes. Despite these promising developments, research in this field is still in its early stages, and many challenges need to be addressed before MeSN-based therapies can be used in clinical settings. Future efforts should focus on improving the biocompatibility and stability of MeSNs, enhancing their ability to target tumors specifically, and ensuring their safety and effectiveness through thorough preclinical and clinical studies. Collaboration across different fields will be crucial to overcome these challenges and unlock the full potential of MeSNs in advanced cancer treatment.

To achieve a meaningful clinical impact, several key issues and challenges for MeSNs still need to be addressed as follows. (1) Limited efficacy: CDT is often limited by the TME. The amount of H_2O_2 and acidity in cancer cells is usually too low to trigger the Fenton/Fenton-like reaction, and high levels of GSH can reduce ROS production. While many MeSNs have been created to address these issues, more advanced and versatile systems are needed to overcome these TME challenges and improve CDT effectiveness. (2) Unclear mechanism: Although the Fenton/Fenton-like reaction for ROS production has been well studied, the precise mechanisms and molecular damage caused by ROS are not fully understood. This gap hinders efforts to improve catalytic efficiency. Gaining a deeper understanding of the CDT process in vivo is essential for advancing cancer treatment. (3) Insufficient stability: Many MeSNs in this field suffer from low stability and high aggregation. Improving their stability for prolonged circulation in the body is crucial for advancing the field. Modifying MeSNs with functional polymers like PEG or using stable organic carriers such as liposomes, dendrimers, and micelles can help achieve this. (4) Inadequate biosafety: The biosafety of MeSNs is crucial for their clinical use. While their biocompatibility has been studied in animal models during treatment, the long-term toxicity is still unclear and needs more research. Biodegradation is important for MeSNs because it allows the body to eliminate them. Therefore, thorough studies on the absorption, distribution, metabolism, and excretion (ADME) of MeSNs are necessary to ensure their safety and future use.

Overall, photo-activated CDT represents a promising approach to improving cancer treatment. It has attracted significant research interest and led to rapid advancements in the field. While various MeSNs have shown excellent photo-enhanced chemodynamic anti-tumor in animal models, more work is needed at both the basic and clinical levels to make these therapies viable for widespread clinical use. Overcoming the remaining challenges will likely accelerate the growth and development of this field.

Author contributions

Conceptualization and supervision: H. J. Investigation, resources, and visualization: H. J. Writing original draft: H. J.,

C. Y., J. Z., T. Y., C. C. H. and T. H. Review and editing: X. J., E. Y. and Z. B.

Data availability

No primary research results, software or code have been included and no new data were generated or analysed as part of this review.

Conflicts of interest

The authors declare no conflicts to declare.

Acknowledgements

Notes and references

1 R. El Khaled El Faraj, S. Chakraborty, M. Zhou, M. Sobol, D. Thiele, L. M. Shatford-Adams, M. Correa Cassal, A.-K. Kaster, S. Dietrich, P. A. Levkin and A. A. Popova, *Adv. Healthcare Mater.*, 2025, **14**, 2401820.

2 B. Cuglievan and V. Subbiah, *Nat. Rev. Clin. Oncol.*, 2025, **22**, 155–156.

3 D. Niraula, K. C. Cuneo, I. D. Dinov, B. D. Gonzalez, J. B. Jamaluddin, J. J. Jin, Y. Luo, M. M. Matuszak, R. K. Ten Haken, A. K. Bryant, T. J. Dilling, M. P. Dykstra, J. M. Frakes, C. L. Liveringhouse, S. R. Miller, M. N. Mills, R. F. Palm, S. N. Regan, A. Rishi, J. F. Torres-Roca, H.-H. M. Yu and I. El Naqa, *Nat. Commun.*, 2025, **16**, 1138.

4 A. S. Cleary, T. L. Leonard, S. A. Gestl and E. J. Gunther, *Nature*, 2014, **508**, 113–117.

5 J. L. Counihan, E. A. Grossman and D. K. Nomura, *Chem. Rev.*, 2018, **118**, 6893–6923.

6 P. Anand, A. B. Kunnumakara, C. Sundaram, K. B. Harikumar, S. T. Tharakan, O. S. Lai, B. Sung and B. B. Aggarwal, *Pharm. Res.*, 2008, **25**, 2097–2116.

7 J. Shi, P. W. Kantoff, R. Wooster and O. C. Farokhzad, *Nat. Rev. Cancer*, 2017, **17**, 20–37.

8 R. S. Riley, C. H. June, R. Langer and M. J. Mitchell, *Nat. Rev. Drug Discovery*, 2019, **18**, 175–196.

9 J. Zhou, L. Rao, G. Yu, T. R. Cook, X. Chen and F. Huang, *Chem. Soc. Rev.*, 2021, **50**, 2839–2891.

10 B. Geng, J. Hu, X. He, Z. Zhang, J. Cai, D. Pan and L. Shen, *Adv. Mater.*, 2024, **36**, 2313670.

11 B. Geng, J. Hu, Y. Li, S. Feng, D. Pan, L. Feng and L. Shen, *Nat. Commun.*, 2022, **13**, 5735.

12 Z. Tang, Y. Liu, M. He and W. Bu, *Angew. Chem., Int. Ed.*, 2019, **58**, 946–956.

13 H. Zhu, W. Zan, W. Chen, W. Jiang, X. Ding, B. L. Li, Y. Mu, L. Wang, S. Garaj and D. T. Leong, *Adv. Mater.*, 2022, **34**, 2200004.

14 H. Zhu, J. Li, X. Qi, P. Chen and K. Pu, *Nano Lett.*, 2018, **18**, 586–594.

15 H. Zhu, Y. Fang, Q. Miao, X. Qi, D. Ding, P. Chen and K. Pu, *ACS Nano*, 2017, **11**, 8998–9009.

16 H. Zhu, B. Li, C. Yu Chan, B. Low Qian Ling, J. Tor, X. Yi Oh, W. Jiang, E. Ye, Z. Li and X. Jun Loh, *Adv. Drug Delivery Rev.*, 2023, **192**, 114644.

17 H. Zhu, J. Zheng, X. Y. Oh, C. Y. Chan, B. Q. L. Low, J. Q. Tor, W. Jiang, E. Ye, X. J. Loh and Z. Li, *ACS Nano*, 2023, **17**, 7953–7978.

18 X. Pan, H. Wang, S. Wang, X. Sun, L. Wang, W. Wang, H. Shen and H. Liu, *Sci. China Life Sci.*, 2018, **61**, 415–426.

19 Y. Zhuang, S. Han, Y. Fang, H. Huang and J. Wu, *Coord. Chem. Rev.*, 2022, **455**, 214360.

20 X. Li, J. F. Lovell, J. Yoon and X. Chen, *Nat. Rev. Clin. Oncol.*, 2020, **17**, 657–674.

21 J. D. Martin, H. Cabral, T. Stylianopoulos and R. K. Jain, *Nat. Rev. Clin. Oncol.*, 2020, **17**, 251–266.

22 L. Zhang, C.-X. Li, S.-S. Wan and X.-Z. Zhang, *Adv. Healthcare Mater.*, 2022, **11**, 2101971.

23 B. Kwon, E. Han, W. Yang, W. Cho, W. Yoo, J. Hwang, B.-M. Kwon and D. Lee, *ACS Appl. Mater. Interfaces*, 2016, **8**, 5887–5897.

24 E. Hwang and H. S. Jung, *Chem. Commun.*, 2020, **56**, 8332–8341.

25 Q. Sun, Z. Wang, B. Liu, F. He, S. Gai, P. Yang, D. Yang, C. Li and J. Lin, *Coord. Chem. Rev.*, 2022, **451**, 214267.

26 P. Manivasagan, A. Joe, H.-W. Han, T. Thambi, M. Selvaraj, K. Chidambaram, J. Kim and E.-S. Jang, *Mater. Today Bio*, 2022, **13**, 100197.

27 X. Wang, X. Zhong, Z. Liu and L. Cheng, *Nano Today*, 2020, **35**, 100946.

28 T. He, X. Qin, C. Jiang, D. Jiang, S. Lei, J. Lin, W.-G. Zhu, J. Qu and P. Huang, *Theranostics*, 2020, **10**, 2453.

29 C. Zhang, D. Li, P. Pei, W. Wang, B. Chen, Z. Chu, Z. Zha, X. Yang, J. Wang and H. Qian, *Biomaterials*, 2020, **237**, 119835.

30 L.-S. Lin, T. Huang, J. Song, X.-Y. Ou, Z. Wang, H. Deng, R. Tian, Y. Liu, J.-F. Wang, Y. Liu, G. Yu, Z. Zhou, S. Wang, G. Niu, H.-H. Yang and X. Chen, *J. Am. Chem. Soc.*, 2019, **141**, 9937–9945.

31 Z. Tang, H. Zhang, Y. Liu, D. Ni, H. Zhang, J. Zhang, Z. Yao, M. He, J. Shi and W. Bu, *Adv. Mater.*, 2017, **29**, 1701683.

32 X. Wang, X. Zhong, H. Lei, Y. Geng, Q. Zhao, F. Gong, Z. Yang, Z. Dong, Z. Liu and L. Cheng, *Chem. Mater.*, 2019, **31**, 6174–6186.

33 B. Ma, S. Wang, F. Liu, S. Zhang, J. Duan, Z. Li, Y. Kong, Y. Sang, H. Liu and W. Bu, *J. Am. Chem. Soc.*, 2018, **141**, 849–857.

34 F. Gong, N. Yang, X. Wang, Q. Zhao, Q. Chen, Z. Liu and L. Cheng, *Nano Today*, 2020, **32**, 100851.

35 F. Jiang, B. Ding, S. Liang, Y. Zhao, Z. Cheng, B. Xing and J. Lin, *Biomaterials*, 2021, **268**, 120545.

36 Y. Liu, W. Zhen, Y. Wang, J. Liu, L. Jin, T. Zhang, S. Zhang, Y. Zhao, S. Song and C. Li, *Angew. Chem., Int. Ed.*, 2019, **131**, 2429–2434.

37 X. Tan, D. Liao, C. Rao, L. Zhou, Z. Tan, Y. Pan, A. Singh, A. Kumar, J. Liu and B. Li, *J. Solid State Chem.*, 2022, **314**, 123352.

38 Y. Pan, Z. Luo, X. Wang, Q. Chen, J. Chen, Y. Guan, D. Liu, H. Xu and J. Liu, *Dalton Trans.*, 2020, **49**, 5291–5301.

39 W. Zhu, J. Zhao, Q. Chen and Z. Liu, *Coord. Chem. Rev.*, 2019, **398**, 113009.

40 P. Horcajada, R. Gref, T. Baati, P. K. Allan, G. Maurin, P. Couvreur, G. Férey, R. E. Morris and C. Serre, *Chem. Rev.*, 2012, **112**, 1232–1268.

41 H. Yu, Y. Yang, T. Jiang, X. Zhang, Y. Zhao, G. Pang, Y. Feng, S. Zhang, F. Wang and Y. Wang, *ACS Appl. Mater. Interfaces*, 2019, **11**, 27536–27547.

42 X. Wang, J. Wang, J. Pan, F. Zhao, D. Kan, R. Cheng, X. Zhang and S.-K. Sun, *ACS Appl. Mater. Interfaces*, 2019, **11**, 33650–33658.

43 L. H. Fu, Y. R. Hu, C. Qi, T. He, S. Jiang, C. Jiang, J. He, J. Qu, J. Lin and P. Huang, *ACS Nano*, 2019, **13**, 13985–13994.

44 C. Xu, J. Li, C. Ou, J. Yang, S. Fu, W. Hu, L. Wang, Z. Wang, L. Hai, L. Deng and D. He, *Chem. Eng. J.*, 2024, **499**, 156170.

45 C. Yao, W. Wang, P. Wang, M. Zhao, X. Li and F. Zhang, *Adv. Mater.*, 2018, **30**, 1704833.

46 M. Saeed, W. Ren and A. Wu, *Biomater. Sci.*, 2018, **6**, 708–725.

47 L. S. Lin, J. Song, L. Song, K. Ke, Y. Liu, Z. Zhou, Z. Shen, J. Li, Z. Yang and W. Tang, *Angew. Chem., Int. Ed.*, 2018, **6**, 708–725.

48 S. Y. H. Wu, K. C. Yang, C. L. Tseng, J. C. Chen and F. H. Lin, *J. Nanopart. Res.*, 2011, **13**, 1139–1149.

49 Y. Chen, G. Zhao, S. Wang, Y. He, S. Han, C. Du, S. Li, Z. Fan, C. Wang and J. Wang, *Biomater. Sci.*, 2019, **7**, 3450–3459.

50 Y. Cheng, Y. Chang, Y. Feng, H. Jian, Z. Tang and H. Zhang, *Angew. Chem., Int. Ed.*, 2018, **57**, 246–251.

51 R. Yang, R. Li, L. Zhang, Z. Xu, Y. Kang and P. Xue, *J. Mater. Chem. B*, 2020, **8**, 7766–7776.

52 W. Fei, Y. Zhang, Y. Ye, C. Li, Y. Yao and Zhang, *J. Mater. Chem. B*, 2020, **8**, 10461–10473.

53 W. Fei, X. Zhang, X. Fan, Y. Ye, M. Zhao, C. Zheng, Y. Li and X. Zheng, *J. Nanobiotechnol.*, 2021, **19**, 93.

54 H. Ranji-Burachaloo, P. A. Gurr, D. E. Dunstan and G. G. Qiao, *ACS Nano*, 2018, **12**, 11819–11837.

55 Z. Tang, Y. Liu, M. He and W. Bu, *Angew. Chem.*, 2019, **131**, 958–968.

56 L. Yang, J. Wang, S. Yang, Q. Lu, P. Li and N. Li, *Theranostics*, 2019, **9**, 3992–4005.

57 G. K. Balendiran, R. Dabur and D. Fraser, *Cell Biochem. Funct.*, 2004, **22**, 343–352.

58 L. S. Lin, J. Song, L. Song, K. Ke, Y. Liu, Z. Zhou, Z. Shen, J. Li, Z. Yang, W. Tang, G. Niu, H. H. Yang and X. Chen, *Angew. Chem., Int. Ed.*, 2018, **57**, 4902–4906.

59 J. Lu, Y. Yang, Q. Xu, Y. Lin, S. Feng, Y. Mao, D. Wang, S. Wang and Q. Zhao, *Coord. Chem. Rev.*, 2023, **474**, 214861.

60 S. Shen, Y. Chao, Z. Dong, G. Wang, X. Yi, G. Song, K. Yang, Z. Liu and L. Cheng, *Adv. Funct. Mater.*, 2017, **27**, 1700250.

61 W. Yin, L. Yan, J. Yu, G. Tian, L. Zhou, X. Zheng, X. Zhang, Y. Yong, J. Li and Z. Gu, *ACS Nano*, 2014, **8**, 6922–6933.

62 S. Q. Li, L. Sun, M. Hou, Q. Chen, R. Yang, L. Zhang, Z. Xu, Y. Kang and P. Xue, *ACS Appl. Mater. Interfaces*, 2018, **11**, 417–429.

63 Q. Z. Lu, L. F.-y. Huang, R. Cao, L. Zhang, G.-h. Tan, N. He, J. Huang, G. Wang and Z. Zhang, *Sci. Rep.*, 2017, 7, 41571.

64 L. Gao, J. Zhuang, L. Nie, J. Zhang, Y. Zhang, N. Gu, T. Wang, J. Feng, D. Yang and S. Perrett, *Nat. Nanotechnol.*, 2007, **2**, 577–583.

65 W. Wang, J. Song, W. Yu, M. Chen, G. Li, J. Chen, L. Chen, L. Yu and Y. Chen, *Adv. Funct. Mater.*, 2024, **34**, 2400929.

66 F. Wu, Q. Zhang, M. Zhang, B. Sun, Z. She, M. Ge, T. Lu, X. Chu, Y. Wang, J. Wang, N. Zhou and A. Li, *ACS Appl. Mater. Interfaces*, 2020, **12**, 10142–10155.

67 J. Wang, Z. Sun, S. Wang, C. Zhao, J. Xu, S. Gao, M. Yang, F. Sheng, S. Gao and Y. Hou, *J. Am. Chem. Soc.*, 2022, **144**, 19884–19895.

68 S. Xiao, Y. Lu, M. Feng, M. Dong, Z. Cao, X. Zhang, Y. Chen and J. Liu, *Chem. Eng. J.*, 2020, **396**, 125294.

69 M. Feng, M. Li, R. Dai, S. Xiao, J. Tang, X. Zhang, B. Chen and J. Liu, *Biomater. Sci.*, 2021, **10**, 258–269.

70 H. Ren, J. Yong, Q. Yang, Z. Yang, Z. Liu, Y. Xu, H. Wang, X. Jiang, W. Miao and X. Li, *Acta Pharm. Sin. B*, 2021, **11**, 3244–3261.

71 M. Zhan, X. Yu, W. Zhao, Y. Peng, S. Peng, J. Li and L. Lu, *J. Nanobiotechnol.*, 2022, **20**, 23.

72 Y. M. Feng, Y. Lu, Y. Yang, M. Zhang, Y. J. Xu, H. L. Gao, L. Dong, W. P. Xu and S. H. Yu, *Sci. Rep.*, 2013, **3**, 2994.

73 G. Guan, X. Wang, B. Li, W. Zhang, Z. Cui, X. Lu, R. Zou and J. Hu, *Nanoscale*, 2018, **10**, 17902–17911.

74 X. Liu, W. Feng, H. Xiang, B. Liu, M. Ye, M. Wei, R. Dong, Y. Chen and K. Dong, *Chem. Eng. J.*, 2021, **411**, 128364.

75 M. B. Gawande, A. Goswami, F. X. Felpin, T. Asefa, X. Huang, R. Silva, X. Zou, R. Zboril and R. S. Varma, *Chem. Rev.*, 2016, **116**, 3722–3811.

76 Y. Li, W. Lu, Q. Huang, M. Huang, C. Li and W. Chen, *Nanomedicine*, 2010, **5**, 1161–1171.

77 M. Wang, H. Zhu, Y. Xue, Y. Duan, H. Tian, Q. Liu, Y. Zhang, Z. Li, X. J. Loh, E. Ye, G. Yin, X. Wang, X. Ding and D. T. Leong, *Bioact. Mater.*, 2024, **42**, 628–643.

78 H. Sun, Y. Zhang, S. Chen, R. Wang, Q. Chen, J. Li, Y. Luo, X. Wang and H. Chen, *ACS Appl. Mater. Interfaces*, 2020, **12**, 30145–30154.

79 R. Hu, Y. Fang, M. Huo, H. Yao, C. Wang, Y. Chen and R. Wu, *Biomaterials*, 2019, **206**, 101–114.

80 Y. Sun, H. Shi, X. Cheng, L. Wu, Y. Wang, Z. Zhou, J. He, H. Y. Chen and D. Ye, *CCS Chem.*, 2020, **3**, 1336–1349.

81 P. Singh, B. Youden, Y. Yang, Y. Chen, A. Carrier, S. Cui, K. Oakes, M. Servos, R. Jiang and X. Zhang, *ACS Appl. Mater. Interfaces*, 2021, **13**, 41464–41472.

82 L. An, C. Wang, Q. Tian, C. Tao, F. Xue, S. Yang, X. Zhou, X. Chen and G. Huang, *Nano Today*, 2022, **43**, 101397.

83 P. M. Zhang, X. Liu, Q. Luo, Q. Wang, L. Zhao, G. Deng, R. Ge, L. Zhang, J. Hu and J. Lu, *Chem. Eng. J.*, 2020, **389**, 124450.

84 J. Yao, F. Yang, F. Zheng, C. Yao, J. Xing, X. Xu and A. Wu, *ACS Appl. Mater. Interfaces*, 2021, **13**, 54770--54782.

85 K. Du, S. Zhao, J. Feng, X. Gao, K. Liu, X. Wang, M. Zhang, Y. Li, Y. Lu and H. Zhang, *J. Mater. Chem. B*, 2021, **9**, 7216–7228.

86 Y. Chen, P. Liu, C. Zhou, T. Zhang, T. Zhou, D. Men, G. Jiang and L. Hang, *Acta Biomater.*, 2023, **158**(1), 649–659.

87 L. S. Li, P. W. Chen, X. J. Zhao, D. Cheng, B. B. Liu, X. J. Tang, W. Q. Zhu, X. Yang and M. X. Zhao, *J. Colloid Interface Sci.*, 2025, **680**, 202–214.

88 S. Wang, A. Riedinger, H. Li, C. Fu, H. Liu, L. Li, T. Liu, L. Tan, M. J. Barthel, G. Pugliese, F. De Donato, M. Scotto D'Abbusco, X. Meng, F. Manna, H. Meng and L. T. Pellegrino, *ACS Nano*, 2015, **9**, 1788–1800.

89 Y. Li, J. Zhou, L. Wang and Z. Xie, *ACS Appl. Mater. Interfaces*, 2020, **12**, 30213–30220.

90 S. Wang, Y. Pang, S. Hu, J. Lv, Y. Lin and M. Li, *Chem. Eng. J.*, 2023, **451**, 138864.

91 Y. Wang, L. An, J. Lin, Q. Tian and S. Yang, *Chem. Eng. J.*, 2020, **385**, 123925.

92 Z. Zhan, W. Zeng, J. Liu, L. Zhang, Y. Cao, P. Li, H. Ran and Z. Wang, *ACS Appl. Mater. Interfaces*, 2023, **15**, 24071–24083.

93 P. An, S. Yin, Y. Qiang, F. Shui, Q. Zhang, C. Zhao, H. Zhou and F. Yu, *New J. Chem.*, 2023, **47**, 16494–16504.

94 Z. Wei, W. Si, M. Huang, M. Lu, W. Wang, C. Liang, X. Dong and Y. Cai, *Adv. Healthcare Mater.*, 2024, **13**, 2402367.

95 H. Hu, W. Zhang, L. Lei, F. Tong, H. Zhang, Y. Zhang, W. Yang, Y. Tang, R. Lin and X. Xia, *Chin. Chem. Lett.*, 2024, **35**, 108765.

96 Y. Yang, W. Zheng, J. Zhang, J. Guo, Q. Liu, H. Wang, F. Xu and Z. Bao, *ACS Appl. Bio Mater.*, 2025, **8**, 676–687.

97 X. Liu, P. Geng, N. Yu, Z. Xie, Y. Feng, Q. Jiang, M. Li, Y. Song, W. Lian and Z. Chen, *J. Colloid Interface Sci.*, 2022, **615**, 38–49.

98 F. Tong, Y. Hu, Y. Xu, Y. Zhou, R. Xie, T. Lei, Y. Du, W. Yang, S. He, Y. Huang, T. Gong and H. Gao, *Acta Pharm. Sin. B*, 2023, **13**, 3471–3488.

99 Y. Cao, L. Jin, S. Zhang, Z. Lv, N. Yin, H. Zhang, T. Zhang, Y. Wang, Y. Chen, X. Liu and G. Zhao, *Eur. J. Pharm. Sci.*, 2023, **180**, 106319.

100 P. Geng, N. Yu, D. K. Macharia, R. Meng, P. Qiu, C. Tao, M. Li, H. Zhang, Z. Chen and W. Lian, *Chem. Eng. J.*, 2022, **441**, 135964.

101 G. Wei, X. Lian, Y. Qin, Y. Zhao, L. Cai, Q. Chen, J.-J. Zou and J. Tian, *Mater. Des.*, 2022, **224**, 111302.

102 M. Sun, D. Yang, W. Fanqi, Z. Wang, H. Ji, Z. Liu, S. Gai, F. Zhang and P. Yang, *J. Mater. Chem. B*, 2020, **8**, 5707–5721.

103 Q. Zou, H. Pan, X. Zhang and and C. Zhang, *J. Mater. Chem. B*, 2023, **11**, 4740–4751.

104 T. Xu, S. Liu, Z. Wei, W. Zhang, G.-Y. Zhang, T. Liu, L. Dai, P. Yin and Y. Song, *ACS Appl. Mater. Interfaces*, 2024, **16**, 14489–14502.

105 L. Kong, F. Yuan, P. Huang, L. Yan, Z. Cai, T. Lawson, W. Wu, S. Chou and Y. Liu, *Small*, 2020, **16**, 2004161.

106 B. Colak, M. C. Cihan and Y. N. Ertas, *ACS Appl. Nano Mater.*, 2022, **6**, 16076–16085.

107 W. Tang, X. Li, Z. Liu, L. Meng, D. Zhu and Q. Huang, *Front. Bioeng. Biotechnol.*, 2022, **10**, 1003777.

108 P. Singh, Y. Chen, B. Youden, D. Oakley, A. Carrier, K. Oakes, M. Servos, R. Jiang and X. Zhang, *Int. J. Pharm.*, 2024, **652**, 123814.

109 M. Moetamani-Ahmadi, A. Mahmoud Ahmadzadeh, M. Alaei, N. Zafari, Z. Negahbanzaferanloo, A. M. Pourbagher-Shahri, F. Forouzanfar, H. Fiuji, H. Mahaki, M. Khazaei, I. S. Gataa, G. A. Ferns, G. J. Peters, J. Batra, A. K.-y. Lam, E. Giovannetti, H. TanzadehPanah and A. Avan, *Int. J. Pharm.*, 2024, **652**, 123839.

110 J. Tao, B. Wang, Y. Dong, X. Chen, S. Li, T. Jiang and X. Zhao, *ACS Appl. Mater. Interfaces*, 2023, **15**, 40267–40279.

111 S. Ning, J. Mo, R. Huang, B. Liu, B. Fu, S. Ding, H. Yang, Y. Cui and L. Yao, *Front. Bioeng. Biotechnol.*, 2023, **11**, 1191014.

112 S. Wu, C. Liu, W. Li, C. Zhang, D. Chen, C. Xu, L. Su and X. Wang, *J. Mater. Chem. B*, 2023, **11**, 2455–2465.

113 Y. He, Y. Pan, X. Zhao, L. Ye, L. Liu, W. Wang, M. Li, D. Chen, Y. Cai and X. Mou, *Chem. Eng. J.*, 2023, **471**, 144410.

114 H. Tian, H. Zhu, Y. Xue, M. Wang, K. Xing, Z. Li, X. J. Loh, E. Ye, X. Ding, B. L. Li, X. Yin and D. T. Leong, *Nanoscale Horiz.*, 2024, **9**, 1190–1199.

115 X. Wang, X. Zhong, Z. Zha, G. He, Z. Miao, H. Lei, Q. Luo, R. Zhang, Z. Liu and L. Cheng, *Applied Materials Today*, 2020, **18**, 100464.

116 L. Zhao, Q. Yang, W. Guo, F. Zhang, K. Yu, C. Yang and F. Qu, *J. Colloid Interface Sci.*, 2021, **600**, 390–402.

117 H. Zhu, S. Huang, M. Ding, Z. Li, J. Li, S. Wang and D. T. Leong, *ACS Appl. Mater. Interfaces*, 2022, **14**, 25183–25196.

118 Y. Jiang, Y. Lu, L. Lei, S. Zhou, L. Yang, X. Yang, Z. Xu, J. Liu and Y. Liu, *Mater. Sci. Eng., C*, 2021, **130**, 112465.

119 X. Li, M. He, Q. Zhou, D. Dutta, N. Lu, B. Li and Z. Ge, *ACS Appl. Mater. Interfaces*, 2022, **14**, 50601–50615.

120 G. Pidamaimaiti, X. Huang, K. Pang, Z. Su and F. Wang, *New J. Chem.*, 2021, **45**, 10296–10302.

121 W. B. Dirersa, G. Getachew, A. Wibrianto, A. S. Rasal, V. S. Gurav, M. Z. Fahmi and J. Y. Chang, *J. Colloid Interface Sci.*, 2023, **647**, 528–545.

122 Z. Mo, M. Qiu, K. Zhao, H. Hu, Q. Xu, J. Cao, Y. Luo, L. Liu, Z. Xu, C. Yi, Z. Xiong, G. Liao and S. Yang, *J. Colloid Interface Sci.*, 2022, **611**, 193–204.

123 S. Liang, G. Liao, W. Zhu and L. Zhang, *Biomater. Res.*, 2022, **26**, 32.

124 G. Ma, X. Zhang, K. Zhao, S. Zhang, K. Ren, M. Mu, C. Wang, X. Wang, H. Liu, J. Dong and X. Sun, *ACS Nano*, 2024, **18**, 3369–3381.

125 J. Lv, X. Wang, X. Zhang, R. Xu, S. Hu, S. Wang and M. Li, *Asian J. Pharm. Sci.*, 2023, **18**, 100798.

126 Y. Lu, Y. Wu, Z. Tang, Y. Hou, M. Cui, S. Huang, B. Long, Z. Yu, M. Z. Iqbal and X. Kong, *Sensors*, 2023, **23**, 8930.

127 T. Han, D. Cui, M. Wu, Q. Sun, Y. Chen, N. Niu and L. Chen, *Microchem. J.*, 2024, **206**, 111466.

128 J. Bao, R. Liu, Z. Yu, Z. Cheng and B. Chang, *Adv. Funct. Mater.*, 2024, **34**, 2316646.

129 J. Ruan, H. Liu, B. Chen, F. Wang, W. Wang, Z. Zha, H. Qian, Z. Miao, J. Sun, T. Tian, Y. He and H. Wang, *ACS Nano*, 2021, **15**, 11428–11440.

130 Y. Zhu, R. Zhao, L. Feng, W. Wang, Y. Xie, H. Ding, B. Liu, S. Dong, P. Yang and J. Lin, *Small Methods*, 2024, **8**, 2400125.

131 Z. Wang, Y. Wang, H. Guo, N. Yu, Q. Ren, Q. Jiang, J. Xia, C. Peng, H. Zhang and Z. Chen, *J. Colloid Interface Sci.*, 2021, **592**, 116–126.

132 M. Wang, Q. Huang, R. Ma, S. Wang, X. Li, Y. Hu, S. Zhu, M. Zhang and Q. Huang, *Colloids Surf., B*, 2024, **234**, 113689.

133 Z. Qin, M. Qiu, Q. Zhang, S. Yang, G. Liao, Z. Xiong and Z. Xu, *J. Mater. Chem. B*, 2021, **9**, 8882–8896.

134 Y. Jiang, Y. Lu, X. Yuan, Y. Zhang, L. Lei, Y. Li, W. Sun, J. Liu, D. Scherman and Y. Liu, *J. Mater. Chem. B*, 2022, **10**, 8082–8093.

135 S. Ma, J. Xie, L. Wang, Z. Zhou, X. Luo, J. Yan and G. Ran, *ACS Appl. Mater. Interfaces*, 2021, **13**, 10728–10740.

136 K. Lv, L. Wang, Y. Ma, F. Zhang, W. Guo, K. Yu, F. Qu and H. Lin, *Biomater. Adv.*, 2022, **136**, 212778.

137 X. Zhu, Z. Chu, B. Chen, Q. Jin, X. Ma, J. Yang, Y. Jiang, W. Wang, Z. Zha and and H. Qian, *Mater. Chem. Front.*, 2022, **6**, 1522–1532.

138 K. Kang, L. Wang, K. Yu, Y. Ma, F. Qu and and H. Lin, *Biomater. Adv.*, 2023, **144**, 213168.

139 L. Wang, K. Kang, H. Hou, Y. Ma, K. Yu, F. Qu and and H. Lin, *J. Colloid Interface Sci.*, 2022, **625**, 145–157.

140 S. Xu, S. Zhou, L. Xie, W. Dou, R. Zhang, B. Zhao, Y. Xu, X. Fu and M. Yuan, *Chem. Eng. J.*, 2023, **460**, 141639.

141 M. Chang, M. Wang, M. Wang, M. Shu, B. Ding, C. Li, M. Pang, S. Cui, Z. Hou and J. Lin, *Adv, Mater*, 2019, **31**, e1905271.

142 Z. Zhou, Z. Gao, W. Chen, X. Wang, Z. Chen, Z. Zheng, Q. Chen, M. Tan, D. Liu, Y. Zhang and Z. Hou, *Acta Biomater.*, 2022, **151**, 600–612.

143 Y. Zhu, Y. Pan, Z. Guo, D. Jin, W. Wang, M. Liu, M. Zong, X. Zheng, Y. Wu, L. Wang, C. Tian, J. Cheng and Y. Liu, *Adv. Healthcare Mater.*, 2023, **12**, 2202198.

144 Z. Liu, N. Zeng, J. Yu, C. Huang and and Q. Huang, *Front. Bioeng. Biotechnol.*, 2022, **10**, 998571.

145 Q. Fang and X. Yin, *J. Nanopart. Res.*, 2023, **25**, 106.

146 X. M. Sun, L. Wang, Y. Zhuo, S. Xu, H. Liu, X. Jiang, Z. Lu, X. Wang, Y. Wang, G. Yue, B. Feng, H. Rao and D. Wu, *Small*, 2024, **20**, 2309593.

147 M. Luo, H. Yukawa, K. Sato, M. Tozawa, M. Tokunaga, T. Kameyama, T. Torimoto and Y. Baba, *ACS Appl. Mater. Interfaces*, 2022, **14**, 34365–34376.

148 Q. Chen, Y. Luo, W. Du, Z. Liu, S. Zhang, J. Yang, H. Yao, T. Liu, M. Ma and H. Chen, *ACS Appl. Mater. Interfaces*, 2019, **11**, 18133–18144.

149 X. Nie, L. Xia, H. L. Wang, G. Chen, B. Wu, T. Y. Zeng, C. Y. Hong, L. H. Wang and Y. Z. You, *ACS Appl. Mater. Interfaces*, 2019, **11**, 31735–31742.

150 Z. W. Tao, Z. Tuo, F. Wu, K. Mu, C. Xu, Y. Shi, Z. Sun, Y. Wang, Y. Li, Z. Zhong, L. Zhou, J. Wang, J. Liu, Y. Du and S. Zhang, *Regener. Biomater.*, 2022, **9**, rbac045.

151 L. Tan, J. Wan, W. Guo, C. Ou, T. Liu, C. Fu, Q. Zhang, X. Ren, X. J. Liang, J. Ren, L. Li and X. Meng, *Biomaterials*, 2018, **159**, 108–118.

152 P. Dash, N. Nataraj, P. K. Panda, C. L. Tseng, Y. C. Lin, R. Sakthivel and R. J. Chung, *ACS Appl. Mater. Interfaces*, 2024, **17**, 222–234.

153 C. Wu, S. Wang, J. Zhao, Y. Liu, Y. Zheng, Y. Luo, C. Ye, M. Huang and H. Chen, *Adv. Funct. Mater.*, 2019, **29**, 1901722.

154 A. Dong, S. Huang, Z. Qian, S. Xu, W. Yuan and B. Wang, *J. Mater. Chem. B*, 2023, **11**, 10883–10895.

155 Y. Luo, L. Zhang, S. Wang, Y. Wang, J. Hua, C. Wen, S. Zhao and H. Liang, *ACS Appl. Mater. Interfaces*, 2023, **15**, 38309–38322.